Interaction between water and point defects inside volume-constrained α-quartz: An *ab initio* molecular dynamics study at 300K

Deep Choudhuri[a,*], Alex J. Rinehart[b,**]

[a]*Department of Materials and Metallurgical Engineering, New Mexico Institute of Mining and Technology, Socorro, New Mexico, 87801*
[b]*Department of Earth and Environmental Science, New Mexico Institute of Mining and Technology, Socorro, New Mexico, 87801*

Abstract

Quartz-based minerals in earth's crust are well-known to contain water-related defects within their volume-constrained lattice, and they are responsible for strength-loss. Experimental observations of natural α-quartz indicate that such defects appear as hydroxyl groups attached to Si atoms, called Griggs defect (Si-OH), and molecular water (H_2O) located at the interstitial sites. However, factors contributing to the formation of Griggs and interstitial H_2O defects remains unclear. For example, the role of point defects like vacancy sites (O^{2-} and Si^{4+}), and substitutional (Al^{3+}) and interstitial (Li^+, K^+, Ca^{2+}, Mg^{2+}, etc.) ions has remained largely unexplored. Here, we performed *ab initio* molecular dynamics at 300K to examine the energetics and structure of water-related defects in volume-constrained α-quartz. Several configurations were systematically interrogated by incorporating interstitial H_2O, O^{2-} and Si^{4+} vacancies, substitutional Al^{3+}, and interstitial Li^+, Ca^{2+} and Mg^{2+} ions within α-quartz. Interstitial H_2O defect was found to be energetically favorable in the presence of Substitutional Al^{3+}, and interstitial Ca^{2+}, Mg^{2+} and Li^{1+}. In the presence of O^{2-} and Si^{4+} vacancies, H_2O showed a strong tendency to dissociate into OH - to form Griggs defect - and a proton; even in the presence of substitutional and interstitial ions. These ions distorted the α-quartz lattice and, in the extreme case, disrupted long-range order to form local amorphous domains; consistent with experimental reports. Our study provides an initial framework for understanding the impact of water within the crystal lattice of an anhydrous silicate mineral such

as quartz. We provide not only thermodynamic and process-related information on observed defects, but also provides guidelines for future studies of water's impact on the behavior of silicate minerals.
Keywords: α-quartz, water defects, *ab initio* molecular dynamics, minerals physics

1. Introduction

Water is present under confinement in a wide range of artificial, biological and geological materials and can have a profound impact on the bulk material properties [1, 2, 3, 4]. Confined water consists of water trapped within nano-scale pores, ranging from a few tenths to tens of nanometers. Confined water has been found to have fundamentally different behavior than bulk water, with properties such as density, dielectric constants, and phase transitions controlled by the interaction of the water with the confining solid [5, 6, 4]. Many of these materials easily incorporate water, often into the crystal lattice or via electrostatically controlled sorption. In many materials, the presence of confined water within the regular lattice or within defects has been observed to decrease strength, possibly via hydrolytic weakening [*] at stress concentrations [7, 8, 9]. However, water is found in interstitial spaces as water-related defects of nominally anhydrous crystal lattices [7, 8, 9, 10, 11, 12, 13, 14, 15]. Among these, α-quartz, or low-temperature quartz, is one of the most common minerals in the Earth's crust and is used in a wide range of applications[7, 8, 9, 10, 11, 12, 13, 14, 15]. It is commonly assumed to be anhydrous, i.e., to not contain water within lattice dislocations, and to primarily exist as water inclusions or small

[*]Corresponding author
[**]Corresponding author
Email addresses: deep.choudhuri@nmt.edu (Deep Choudhuri), alex.rinehart@nmt.edu (Alex J. Rinehart)
[*]Loss of mechanical strength in rocks and minerals due to the presence of water

bubbles [7, 8, 9, 10, 11, 12, 13, 14, 15, 16]. However, confined water in quartz lattice defects have been observed via FTIR techniques since the 1980s, including hypothesized but not verified structures [7, 8, 9, 10, 11, 12, 13, 14, 15, 16]. This study focused on the energetics and structure of a suite of water-related defects in the α-quartz crystal lattice by performing ab initio atomistic simulations at a low temperature of 300K.

In α-quartz, three types of water-related defects have been documented using infrared spectroscopy and electron microscopy. [7, 8, 9, 10, 15, 16, 17, 18, 12, 13, 14]. The *first* type of defect is called "Griggs" defect, where an hydroxyl (OH^-) group attaches itself to a Si or the bridging O atom in Si-O-Si via hydrolysis [7, 8, 9]. They are thought to be unstable in mechanically unconstrained α-quartz, and their formation in the presence of preexisting vacancies (Si^{4+} or O^{2-}) is yet to be examined in at finite temperatures [19, 13, 14]. *Second* is a hydrogarnate-type defect, or hydrogarnate: It forms by the interaction between four protons (H^+) with a Si^{4+} vacancy site, and results in four new hydroxyl groups [10, 13, 14]. It is worth noting that Griggs and hydrogarnate defects notionally excludes the presence of molecular water (H_2O) as defects within quartz-lattice; they only consider defects with water in it's *dissociated state*.

Later, Stenina proposed a *third* defect-type based on transmission electron microscopic observations of naturally occurring alpha-quartz minerals. In these third defect types, undissociated H_2O exists within the interstices of an α-quartz lattice [12]. (In the α-quartz lattice, interstitial sites form a cage-like volume that comprise Si-O-Si bonds). Furthermore, their studies indicated that such interstitial H_2O coexists with O^{2-} vacancies, where charge-compensating impurity atoms occupy lattice and interstitial sites [12].

Several types of impurity elements can occupy the lattice and interstices of α-quartz. They

include monovalent (e.g., Li^+, Na^+, K^+), divalent (Ca^{2+}, Mg^{2+}, Fe^{2+}), and trivalent (Al^{3+}, Fe^{3+}) cations [12, 13]. Among these Al^{3+} and Li^+ are thought to be most prevalent. Typically, Al^{3+} substitutes Si^{4+}, and Li^+ are present at the interstitial spaces as charge compensating species [12, 13]. Stenina further demonstrated that the presence of molecular H_2O, along with impurities, disrupted the crystalline order of quartz, and formed amorphous domains within the host lattice [12]. Notwithstanding, extant water-related defect studies indicate that formation of water-related defects within the quartz lattice is closely associated with atomic point defects, i.e., vacancy, substitution and interstitial, and is well-known in the geology literature [10, 12, 13].

Interestingly, despite a significant body of literature - spanning nearly seven decades - on water-related defects in α-quartz [7, 8, 9, 10, 11, 15, 18, 12, 13], limited *ab initio* studies were performed on this topic [20, 19, 21, 22, 14]. Earliest DFT studies focused on pure α-quartz. One of them suggested that presence of molecular water within α-quartz and hydrolysis of Si-O-Si (Griggs defect) are energetically unfavorable, and water-related defects corresponds to hydrogarnate-type structure [22]. A latter study clarified that Griggs defect is stable within α-quartz lattice, and further elaborated on the structure and existence of hydrogarnate-type defect [14]. They also examined charged systems and effect of interstitial impurities [14].

Notwithstanding, existing computational studies share three key characteristics [20, 19, 21, 22, 14]. They employed density functional theory (DFT)-based first principles calculations. Initial geometries were chosen by appropriately placing OH or H next to Si atoms or Si-O-Si bonds, and, subsequently, they were optimized using well-known energy-minimizing algorithms. These methods result in structures that are stable at 0K (see [23] and [24] for a description of those algorithms). Defect structure proposed by Stenina remains largely unexamined using computational

tools. High temperature simulations are readily performed using classical Molecular Dynamics (MD) [25, 23, 26]. However, they are limited by the availability of semiempirical potentials that can describe interatomic interactions between arbitrary elements, e.g., bond formation and reconstruction between different species. [23, 26, 27].

Here, we have performed *Ab Initio* Molecular Dynamics (AIMD) simulations at 300K to probe the structure and energetics of water-related defects in α-quartz. The choice of methodology was guided by three reasons: *first*, AIMD allows interrogation of structural changes involving bond breaking or formation [28, 29, 30, 25, 31, 32, 27],e.g., dissociation of water; *second*, it permits incorporation of arbitrary elements, whose semiempirical potentials are currently unavailable for conducting classical MD[33, 34]; and, *third*, facilitates the probing interatomic interactions in a charged environment at a non-zero temperature [33, 34]. Our model system involves systematic examination of several defect configurations, where H_2O molecules are embedded within α-quartz lattice, and, subsequently, probing their interactions with Si-O-Si bonds presence of Si^{4+} and O^{2-} vacancies, and impurity species like Al^{3+}, Li^{+}, Ca^{2+}, and Mg^{2+}. Furthermore, to mimic natural conditions, these defect configurations examined within a volume-constrained α-quartz lattice, whose lattice parameters were fitted to those of pure specimen at 300K.

The remainder of the manuscript is organized into three sections: simulation details are presented in *Section*.2, results in *Section*.3, and, finally, in *Section*.4 we discuss the implication of our results within the context of defect stability and their population.

2. Computational methods

2.1. Simulation details

Atomistic simulations was performed using the Vienna Ab-initio Simulation Package (VASP), which employs projector augmented plane-wave (PAW) method; and, allows the description of electron exchange correlation functional through generalized gradient approximation (GGA) by using Perdew-Burke-Ernzerhof (PBE) parameterization [35, 36, 37, 38, 39, 40]. *Ab initio* MD (AIMD) simulations were based-on Born-Oppenheimer dynamics, which allowed us to compute atomic forces of canonical ensembles, i.e. constant number of particles (N), volume (V) and temperature (T) [41, 26]. Equations of motion were solved using a time-step Δt=0.001 picoseconds (ps) or 1×10^{-15}s, and the temperature was nominally maintained a 300K using the Andersen thermostat [42]. Through systematic testing we found that collision frequency ν=0.01-0.05 gave consistent results i.e., the coupling strength between temperature bath and system. Our choice of ν is consistent with literature reports [43, 44, 45, 46]: They prescribe smaller *nu* values, because that minimizes alteration of phase-space trajectories from stochastic collisions. The application of Andersen thermostat does not present any significant hurdles as long as atomic trajectories were not utilized for computing deterministic dynamical properties like the diffusion coefficients [42, 47, 45, 46]. However, the stochastic nature of this thermostat allows the resultant dynamics to acquire uniform ergodicity [42, 48]. Therefore, Andersen thermostat can be reliably use for computing energies and examining equilibrium structures [47, 49, 50, 51, 52] - a key requirement of this study.

Electronic degrees of freedom in AIMD simulations was computed by using 560eV plane-

wave cut-off energy and global convergence of 0.01eV. Brillouin zone was sampled using 2×2×4 (or, 0.35 $Å^{-1}$ k-spacing) mesh centered at Γ point, partial occupancy of orbitals were described using the tetrahedron method with Blöchl corrections, 0.04 eV smearing width, and the electronic iterations was limited via 10^{-4}eV threshold. Dispersion correction, due to van der Waals interactions, was incorporated using the DFT-D2 method that was proposed by Grimme [53, 54, 55]. Next, we describe the geometry of simulation box, and the initial configurations used employed in the simulations.

2.2. Model geometries utilized in AIMD simulations

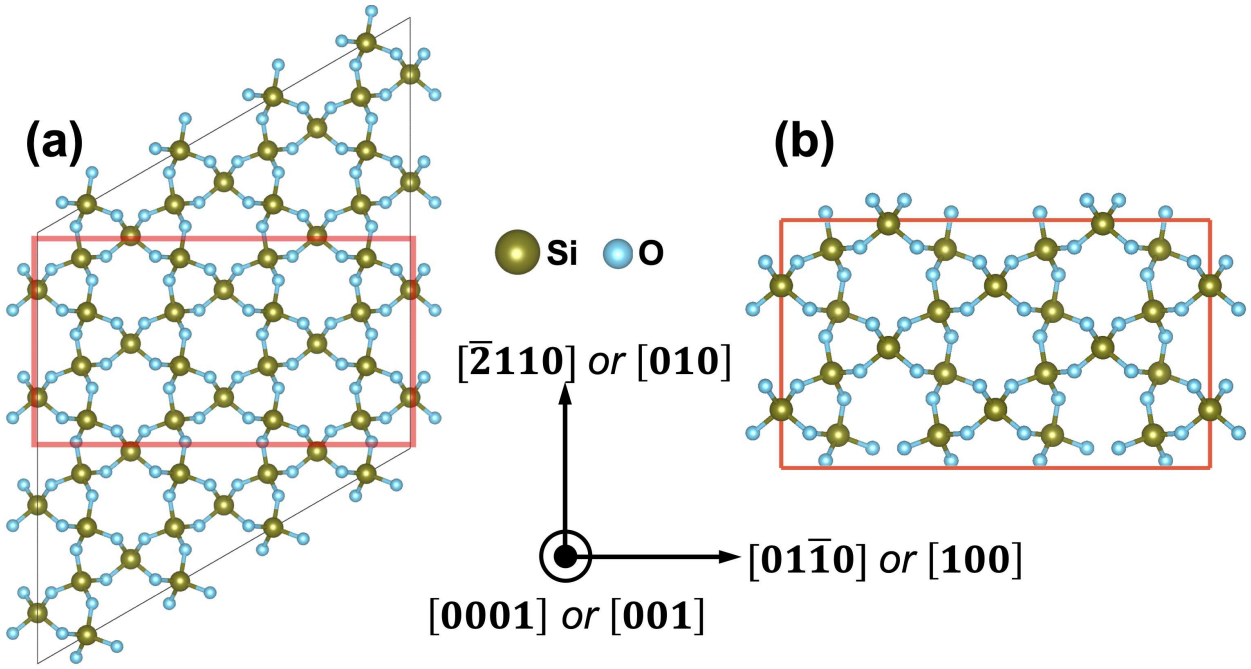

Figure 1: Depiction of α-quartz geometry: (a) supercell showing the trigonal structure of the α-quartz viewed along [0001] direction, and the red colored box indicates an orthogonal motif; (b) supercell corresponding to the orthogonal motif, where the in-plane x and y axes are oriented along [$\bar{2}$110] and [01$\bar{1}$0]. This orthogonal supercell or the simulation box was employed in AIMD simulations.

The trigonal crystal structure (hexagonal lattice) of alpha-quartz, or α-SiO_2, can be described using a $P3_221$ space group [56, 57, 58, 59]. Experimentally observed lattice parameters are nomi-

nally $a = b = 4.92$Å, c=5.41Å, α=β=90°, and γ=120° [60, 56, 57, 58, 59, 61, 14]. Fig.1a shows the trigonal structure of α-SiO_2, where the unit cell is replicated 4 times along [100] (or [01$\bar{1}$0]) and [010] (or [$\bar{2}$110]) directions and once along [001], i.e., 4×4×1, to form a supercell. Subsequently, a 72 atom orthogonal supercell was extracted from that trigonal supercell, where the orthogonal X, Y and Z axes were oriented parallel to [100], [010] and [001], respectively - see Fig.1b. This orthorombic supercell was energy minimized by using the conjugate gradient algorithm, which relaxed ionic positions, shape and volumetric degrees of freedom. This specific calculation employed 10^{-7}eV threshold for carrying out Brillouin zone integration, and a global convergence criterion of 10^{-3} eV. Notionally, such energy minimization yields a relaxed structure, corresponding to 0K [23, 24]; hereafter, called 0K-DFT. Appendix A show our computed 0K-DFT values, which are consistent with literature [22, 14, 62].

Subsequently, the 0K-DFT structure was equilibrated at 300K using NVT ensemble for 5ps (see *Section*.2.2). In our AIMD simulations, the average external pressure ($\langle P^{ext} \rangle$) on the supercell was maintained at 0.03GPa (i.e., nominally zero GPa) by systematically changing lengths of the supercell lattice vectors [32, 27]. In reference to the crystallographic axes shown in Fig.1, the final AIMD-equilibrated supercell dimensions were 9.755, 16.840 and 5.280Å along [100], [010] and [001], respectively. This starter orthogonal supercell was the basis for creating simulations of 23 initial, "defect-implanted" configurations studied (see Table.1). The number of atoms in these supercell configurations ranged from 72-78. AIMD-NVT simulations of those configurations were performed by constraining their volume to pure α-SiO_2 (V^{α}), that had been previously equilibrated at 300K and $\langle P^{ext} \rangle \sim$0GPa.

Broadly, three categories of configurations were considered for simulations, and supercells

Table 1: List of initial configurations utilized for AIMD simulations. Here, "Charge neutral" means charge neutralization was achieved by adding extra ions, while "Charge compensated" indicates that neutralization was enforced by VASP via background charge compensation.

Configuration	**Defect type**[a]	**Remarks**
W_ in	(1) interstitial H_2O molecule	Charge neutral
2W_ in	(2) interstitial H_2O molecules	Charge neutral
W_ in_O-vac	(1) interstitial H_2O molecule, and (1) O^{2-} vacancy	Charge compensated
W_ in_Si-vac	(1) interstitial H_2O next to (1) Si^{4+} vacancy	Charge compensated
2W_ in_Si-vac	(2) interstitial H_2O next to (1) Si^{4+} vacancy	Charge compensated
4H_Si-vac_1	(1) Si^{4+} vacancy and (4) charge compensating H	Charge neutral
4H_Si-vac_2	(1) Si^{4+} vacancy and (4) charge compensating H	Different H locations
AlLi	(1) interstitial H_2O, (1) Al^{3+} substituting Si^{4+}, and (1) interstitial Li^+	Charge neutral
AlLi_O-vac	(1) interstitial H_2O, (1) O^{2-} vacancy, (1) Al^{3+} substituting Si^{4+}, and (1) interstitial Li^+	Charge compensated
2Al2Li	(1) interstitial H_2O, (1) O^{2-} vacancy, (2) Al^{3+} substituting Si^{4+}, and (2) interstitial Li^+	Charge neutral
2Al2Li_O-vac	(1) interstitial H_2O, (2) Al^{3+} substituting Si^{4+}, and (2) interstitial Li^+	Charge compensated
2Al4Li_O-vac	(1) interstitial H_2O, (1) O^{2-} vacancy, (2) Al^{3+} substituting (2) Si^{4+}, and (4) interstitial Li^+	Charge neutral
Al3Li_O-vac_1	(1) interstitial H_2O, (1) O^{2-} vacancy, (1) Al^{3+} substituting (1) Si^{4+}, and (3) interstitial Li^+	Charge neutral
Al3Li_O-vac_2	(1) interstitial H_2O, (1) O^{2-} vacancy, (1) Al^{3+} substituting (1) Si^{4+}, and (3) interstitial Li^+	Different Li^+ location,charge neutral
2Li_O-vac	(1) interstitial H_2O, (1) O^{2-} vacancy, and (2) interstitial Li^+	Charge neutral
Ca2Al2Li_O-vac	(1) interstitial H_2O, (1) O^{2-} vacancy, (2) Al^{3+} substituting (2) Si^{4+}, (2) interstitial Li^+, and (1) interstitial Ca^{2+}	Charge neutral
CaAlLi_O-vac_1	(1) interstitial H_2O, (1) O^{2-} vacancy, (1) Al^{3+} substituting (1) Si^{4+}, (1) interstitial Li^+, and (1) interstitial Ca^{2+}	Charge neutral
CaAlLi_O-vac_2	(1) interstitial H_2O, (1) O^{2-} vacancy, (1) Al^{3+} substituting (1) Si^{4+}, (1) interstitial Li^+, and (1) interstitial Ca^{2+}	Different Ca^{2+} location, charge neutral
Mg2Al2Li_O-vac	(1) interstitial H_2O, (1) O^{2-} vacancy, (2) Al^{3+} substituting (2) Si^{4+}, (2) interstitial Li^+, and (1) interstitial Mg^{2+}	Charge neutral
MgAlLi_O-vac_1	(1) interstitial H_2O, (1) O^{2-} vacancy, (1) Al^{3+} substituting (1) Si^{4+}, (1) interstitial Li^+, and (1) interstitial Mg^{2+}	Charge neutral
MgAlLi_O-vac_2	(1) interstitial H_2O, (1) O^{2-} vacancy, (1) Al^{3+} substituting (1) Si^{4+}, (1) interstitial Li^+, and (1) interstitial Mg^{2+}	Different Mg^{2+} location, charge neutral
CaMg2Al2Li_O-vac	(1) interstitial H_2O, (1) O^{2-} vacancy, (2) Al^{3+} substituting (2) Si^{4+}, (2) interstitial Li^+, (1) interstitial Mg^{2+} , and (1) interstitial Ca^{2+}	Charge compensated
CaMgAlLi_O-vac_2	(1) interstitial H_2O, (1) O^{2-} vacancy, (1) Al^{3+} substituting (1) Si^{4+}, (1) interstitial Li^+, (1) interstitial Mg^{2+} , and (1) interstitial Ca^{2+}	Charge compensated

[a] Number of defects are indicated inside the parenthesis.

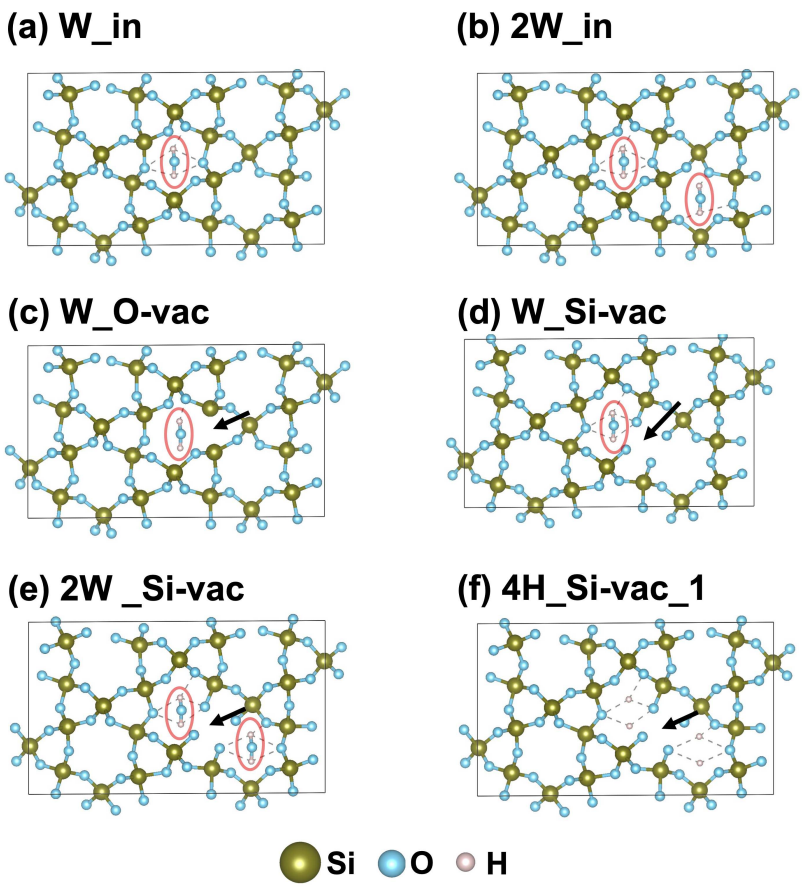

Figure 2: Initial configurations used for simulating water-related defects in pure α-quartz: (a) single H_2O located inside Si-O-Si cage; (b) two H_2O inside Si-O-Si cage; (c) single H_2O located near an O vacancy; (d) single H_2O located near an Si vacancy; (e) two H_2O near a Si vacancy; and, (f) four hydrogen atoms near a Si vacancy. O and Si vacancies are indicated with an arrow in panels "c-d", while H_2O molecules are marked with ovals. Structures were prepared using VESTA [63].

corresponding to those configurations are shown in Figs.2, 3, and 4. The *first* category involves incorporating an interstitial H_2O, and O^{2-} and Si^{4+} vacancies inside the Si-O-Si cages of "pure" α-SiO_2. We used W_*in* (Fig.2a) and 2W_*in* (Fig.2b) to examine the interaction of one and two H_2O molecules with Si-O-Si bonds, respectively; W_*in*O-vac examined the effect of O^{2-} vacancy on H_2O (Fig.2c); W_Si-vac (Fig.2d) and 2W_Si-vac (Fig.2e) was used to examine the interaction of one and two H_2O molecules with Si-O-Si bonds, respectively; and, (Fig.2f) 4H_Si-vac will be used to understand how four H atoms (protons) interact with a Si vacancy (Table.1). The 4H_Si-

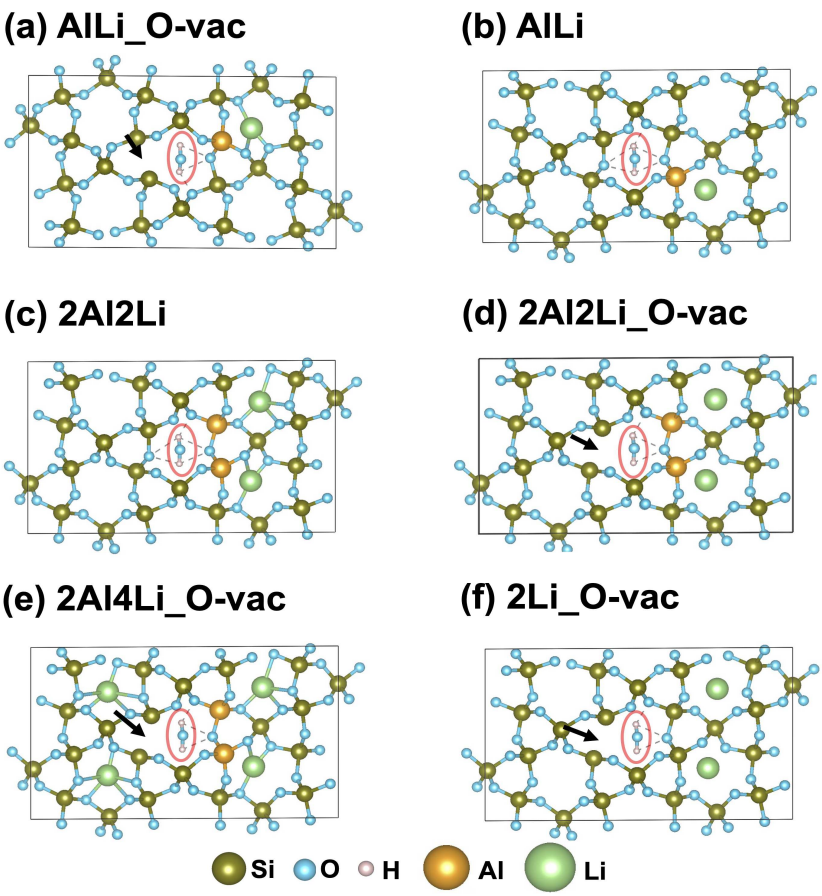

Figure 3: Initial configurations used for simulating water-related defects in α-quartz that contains substitutional trivalent-Al and interstitial monovalent-Li atoms: (a) H_2O near Al, Li and O vacancy (AlLi_O-vac); (b) H_2O near Al and Li (AlLi); (c) H_2O near two Al and Li (2Al2Li); (d) H_2O near two Al, two Li and O vacancy (2Al2Li_O-vac_1); (e) H_2O near two Al, four Li and O vacancy (2Al4Li_O-vac); (f) H_2O near two Li and O vacancy (2Li_O-vac). O vacancy is indicated with an arrow, while H_2O molecules are marked with ovals. Structures were prepared using VESTA [63].

vac configuration will evaluate if AIMD can reproduce the hydrogarnate structure, i.e.,with four Si-OH ends, which is often reported in literature concerning "water" defects in α-SiO_2 [13, 14].

The next two categories examined the effect of chemical impurities, with or without O^{2-} vacancy, on the interaction of interstitial H_2O with its surrounding Si-O-Si cage. (We will not include "*_in*" in "naming" the second and third category configurations, because all structures contain interstitial H_2O). Fig.3 exemplifies configurations considered in the *second category*, where trivalent

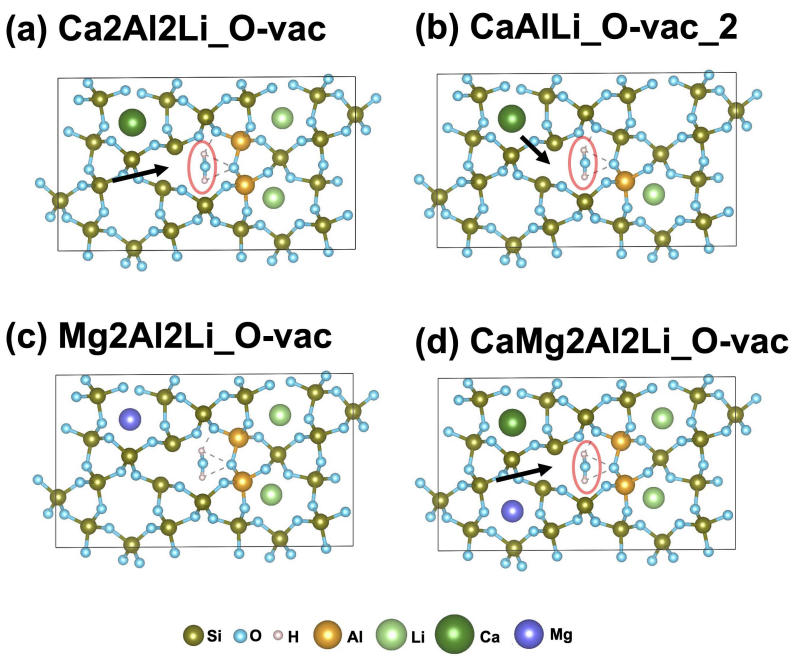

Figure 4: Initial configurations used for simulating water-related defects in α-quartz that contains substitutional trivalent-Al, interstitial monovalent (Li) and divalent (Ca and Mg) atoms: (a) H_2O near two Al, two Li, one Ca and O vacancy (Ca2Al2Li_O-vac); (b) H_2O near Al, Li, Ca and O vacancy (CaAlLi_O-vac_2); (c) H_2O near two Al, two Li, one Mg and O vacancy (Mg2Al2Li_O-vac); and (d) H_2O near two Al, two Li, one Mg, one Mg and O vacancy (CaMg2Al2Li_O-vac). O vacancy is indicated with an arrow, while H_2O molecules are marked with ovals. Structures were prepared using VESTA [63].

Al^{3+} ions substitute tetravalent Si^{4+} sites and Li^+ monovalent ions occupy interstitial sites. From a charge balance standpoint, substituting one Si^{4+} site with a Al^{3+} results in net, one negative charge in the structure. Li^+ was added to neutralize that charge. One configuration without Al^{3+} substitution, and containing Li^+ ions and O^{2-} vacancy - 2Li_O-vac designation - was also included in the second category (see Table.1). Fig.4 shows the *third category* of supercell configurations, where Ca^{2+} and Mg^{2+} divalent ions were added to structures containing prior Al^{3+} substitution and Li^+ interstitial. The selection of Al, Li, Ca and Mg was guided by their relatively high abundance in α-SiO_2 [12, 13, 64]. (In Figs.3 and 4, the bonds between the interstitial Ca^{2+}, Mg^{2+} and Li^+, and their surrounding are not shown in order to highlight their interstitial nature. This depiction will

be maintained throughout the manuscript). Finally, we note that our choices were filtered on the basis of energy considerations (see *Sections*. 3.1 and 3.2), guidance from extant literature, e.g., O^{2-} vacancies are usually the first nearest neighbors of impurity atoms [12, 14], and computational demands required to perform AIMD simulations involving multi-element configurations.

Lastly, charge neutralization or compensation in W_ in_O-vac, W_ in_Si-vac, 2W_ in_Si-vac, and AlLi_O-vac was not performed by adding ions to the structure (see Table.1, and Figs.2 and 3). Instead, charge compensation was performed by adjusting the total number of electrons. VASP implements this via the "NELECT" tag, which assumes a neutralizing background charge.

2.3. Methods for analyzing simulation results

Structures obtained from AIMD simulations were visualized using VESTA, while Ovito was employed for computing radial distribution functions[63, 65]. All simulations were performed till energy convergence was achieved, and the last 1ps was conservatively chosen for examining structures, and computing average internal energy ($\langle \mathcal{U} \rangle$) and internal pressure ($\langle P^{int} \rangle$). We demonstrate the rationale for these choices of time domains to calculate equilibrium conditions within in Fig.5, which shows internal energy ($\mathcal{U}$) v.s. simulation time for W_in and CaAlLi_O-vac_2. In the last 1ps (e.g. see shaded region in Fig.5), we found that the structure and pressure remained largely unchanged.

Thermodynamic stability at 300K was estimated by computing enthalpy of formation, and defect formation energies of each configuration. Enthalpy of formation ($\Delta H^{i}_{supercell}$) was computed

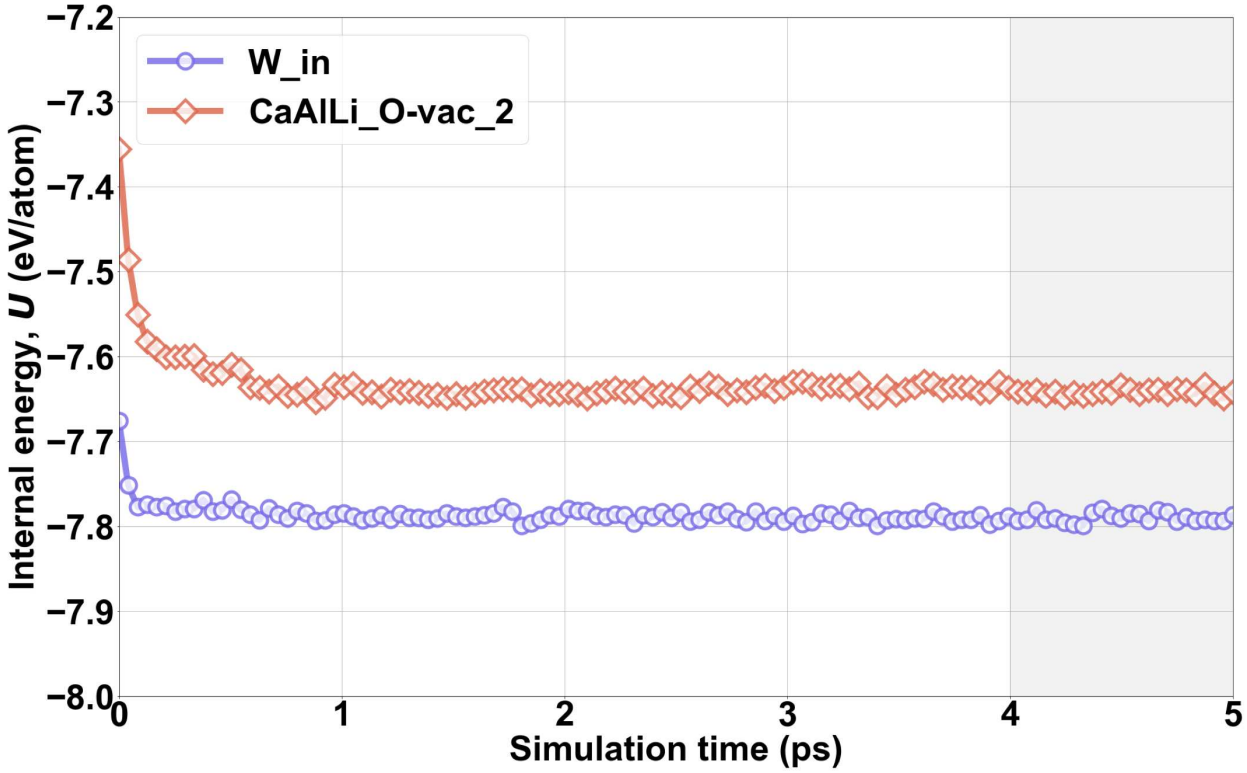

Figure 5: Plots showing the variation in AIMD-computed internal energy ($\mathcal{U}$) with time for two example configurations at 300K. The shaded region between 4-5ps indicates energy convergence and that system has achieved local equilibrium. $\mathcal{U}$ in that time duration was conservatively used for obtaining average values, and enthalpy of defect formation

using the formula:

$$\Delta H^{i}_{supercell} = \frac{1}{N_{Total}}\langle H^{i}\rangle - \left\{\frac{n_{Si}}{N_{Total}}\langle \Delta H^{diamond\ cubic}_{Si}\rangle + \frac{n_{O}}{N_{Total}}\langle \Delta H^{diatom}_{O}\rangle + \frac{n_{H}}{N_{Total}}\langle \Delta H^{diatom}_{H}\rangle\right\}^{\alpha-quartz}_{constituents} - \left\{\frac{n_{Al}}{N_{Total}}\langle \Delta H^{FCC}_{Al}\rangle + \frac{n_{Li}}{N_{Total}}\langle \Delta H^{BCC}_{Li}\rangle + \frac{n_{Ca}}{N_{Total}}\langle \Delta H^{FCC}_{Ca}\rangle + \frac{n_{Mg}}{N_{Total}}\langle \Delta H^{HCP}_{Mg}\rangle\right\}_{impurities} \tag{1}$$

where, $\langle \Delta H^{i}\rangle$ is enthalpy of the supercell corresponding to the ith defect configuration; $\langle ...\rangle$ represents average value, and, in general $\langle H\rangle = \langle \mathcal{U}\rangle + \langle P^{int}\rangle \times V^{\alpha}$ [41, 66], where $\langle P^{int}\rangle$ is the internal pressure resulting from constraining ith configuration to the volume V^{α} of pristine α-SiO_2 at

300K (see *Section*.2.2); $\langle \Delta H_{Si}^{diamond\ cubic} \rangle$, $\langle \Delta H_{O}^{diatom} \rangle$, $\langle \Delta H_{H}^{diatom} \rangle$, $\langle \Delta H_{Al}^{FCC} \rangle$, $\langle \Delta H_{Li}^{BCC} \rangle$, $\langle \Delta H_{Ca}^{FCC} \rangle$, and $\langle \Delta H_{Mg}^{HCP} \rangle$ the reference enthalpy of contributing elements in their stable states at 300K and ambient pressure, i.e., diamond cubic for Si, face-centered cubic (FCC) for Al and Ca, body-centered cubic (BCC) for Li, hexagonal closed packed (HCP) for Mg, and diatomic molecules for H and O; n_{Si}, n_O, n_H, n_{Al}, n_{Li}, n_{Ca}, and n_{Mg}, are the number of Si, O, H, Al, Li, Ca and Mg atoms, respectively, present in the ith configuration; and, $N_{Total} = n_{Si} + n_O + n_H + n_{Al} + n_{Li} + n_{Ca} + n_{Mg}$. Appendix.B provides a detailed derivation of eq.1. The formulation of eq.1 provides a robust and consistent framework for comparing configuration energetics with respect to pure elements, only. Importantly, it quantifies the thermodynamic feasibility of forming such structures as bulk materials at 300K.

However, structures presented in *Section.*2.2 will likely be present as defects within pristine bulk α-SiO_2 in minute quantities. Therefore, we have *estimated* defect formation energy at 300K using the expression:

$$\Delta H_{defect}^{i} = \frac{\langle \mathcal{U}^{i} \rangle}{N_i} - \frac{\langle \mathcal{U}^{\alpha - SiO_2} \rangle}{N_{\alpha - SiO_2}} \tag{2}$$

where, $\langle \mathcal{U}^{i} \rangle$ and $\langle \mathcal{U}^{\alpha - SiO_2} \rangle$ are the internal energies of the i^{th} defect configuration and pristine α-SiO_2, respectively; while, N_i and $N_{\alpha - SiO_2}$ are number of atoms within the i^{th} configuration and defect-free α-SiO_2 supercells, respectively. Notionally, eq.2 measures per atom energy differences with respect to bulk α-SiO_2. This energy difference implicitly includes the effect of misfit strain required to incorporate a defect configuration within a pristine lattice at 300K, because the supercell dimensions of defect configurations were constrained to that of pristine α-SiO_2. During

equilibration at 300K, the defect structures will locally expand or contract the surrounding SiO_2 cages. Such local deformations will impart pressure/stress to the overall supercell, which is captured in eq.2; meaning, ΔH^{i}_{defect} is implicitly also a function of strain energy. It is worth noting that such supercell pressure is also incorporated in eq.1 (see Appendix.B). Taken together, eqs.1 and 2 allowed us to reasonably assess the energetics of defect configurations with and without impurities.

The "global" structure around defects were probed using the radial distribution function (RDF) [67]:

$$g(r) = \frac{1}{\rho N_{Total}} \left\langle \sum_{m}^{N_{Total}} \sum_{m \neq n}^{N_{Total}} \delta[r - r_{mn}] \right\rangle, \tag{3}$$

where, N_{Total} is the total number of atoms in the supercell, ρ is the density of the supercell ($=\frac{N_{Total}}{V^{\alpha}}$), r_{mn} is the distance between centers of m^{th} and n^{th} atoms, r is the distance of shell from a reference central particle, e.g., the m^{th} atom, and δ is the delta function. Eq.3 allowed us to evaluate the overall influence of water-related defects on the structure of volume-constrained α-SiO_2 at 300K.

3. Results

Simulations results are divided into two subsections, where we will focus on water-related defects that were equilibrated at 300K. *Section*.3.1, examines the interaction of interstitial H_2O with O^{2-} and Si^{4+} vacancies in α-SiO_2, and *Section*.3.2 compares and contrasts such interactions in the presence of chemical impurities, i.e., Al^{3+} substitutions at prior Si^{4+} sites and Li^{+}, Ca^{2+} and Mg^{2+} interstitial cations within volume-constrained α-SiO_2.

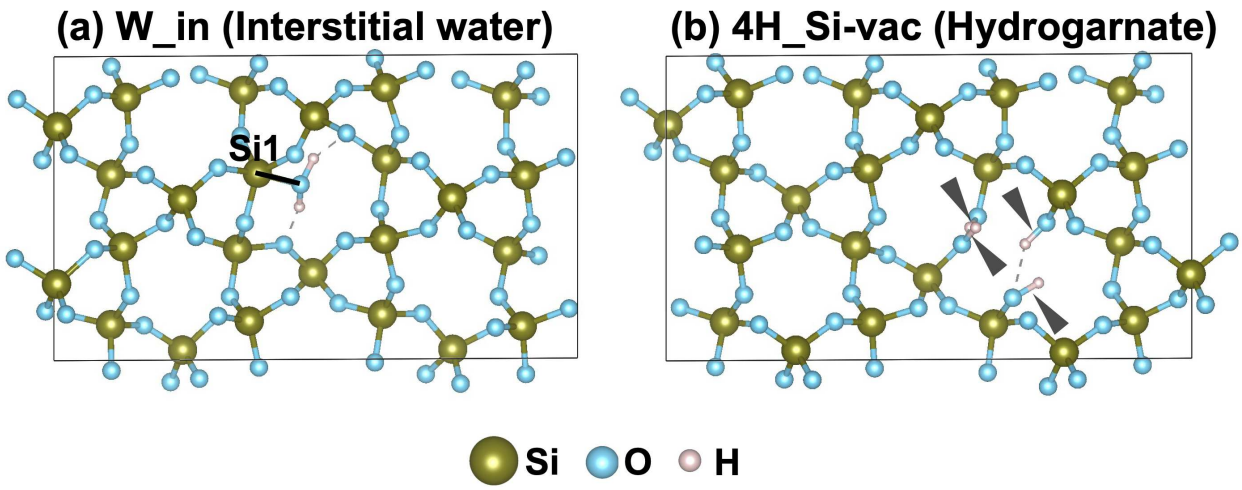

Figure 6: AIMD snapshots at 5ps show (a) the presence of interstitial water inside the Si-O-Si cage (W_in), and (b) hydroxyl (OH) groups bonded to four Si atoms, i.e., a hydrogarnate structure (4H_Si-vac) [11, 22, 13, 14]. The dotted lines in panels "a" and "b" represent hydrogen bonds, the solid line in "a" shows the shortest distance between a Si atom and O in interstitial water.These results demonstrate that interstitial water and hydrogarnate structure are stable defects at 300K.

3.1. Water defects in pure SiO_2 at 300K

Two types of defects were first examined that have received attention in 0K-DFT literature (employing energy minimization approaches) [20, 19, 21, 22, 14], and, subsequently, compared them with our AIMD results. Such defects are caused by interstitial H_2O, and presence of prior Si^{4+} vacancy (also called *hydrogarnate* and indicated using $(4H)^{\times}_{Si}$ in literature [10, 13, 14]); here, we designated them using W_in and 4H_Si-vac, respectively (see Table.1 and Fig.2 for the description of initial structures). Fig.6 shows the defect structures with α-SiO_2 after equilibrating at 300K for 5ps. Fig.6a shows that a H_2O molecule lodged next to Si atom (marked as Si1). The distance between the O atom in H_2O and Si1 (indicated with a black line) varied between 1.88-2.04Å, within the last 1ps simulation timeframe (shaded region in Fig.5). Crucially, Fig.6a shows that interstitial H_2O does not dissociate at 300K, which is comparable to the static 0K-DFT results reported by Jollands *et.al.* [14]. Fig.6b shows a hydrogarnate defect at 300K comprising four

OH groups - indicated with black arrow heads - that are located near a site of prior Si^{4+} vacancy (compare with Fig.2d). In this 5ps snapshot, the OH bond-lengths varied between 0.95-9.98Å, which is comparable to extant reports [22, 14]. Broadly, Fig.6 demonstrates that our AIMD results are consistent with literature, and interstitial H_2O and hydrogarnate defects are structurally stable (even for a very short duration) within volume-constrained α-SiO_2 at 300K.

Additionally, the literature reports the presence of OH defects within the lattice of α-SiO_2 [11, 13]. 0K-DFT studies examined such defects by *a priori* inserting a vacancy and "appropriately" protons in the starting, pre-energy minimized, configurations [22, 14]. In fact, the 4H_Si-vac was obtained by placing a Si^{4+} defect in it's initial configuration along with four protons (see Fig.2d). Interestingly, stability of an interstitial H_2O located near O^{2-} or Si^{4+} vacancy was yet to be examined using DFT-based techniques. Therefore, we have probed the effect of such point defects on the structural stability of interstitial H_2O.

AIMD snapshots of defect structures with prior O^{2-} and Si^{4+} vacancies are presented in Fig.7a1 (W_O-vac) and Fig.7b1-c1 (W_Si-vac and 2W_Si-vac), respectively. W_Si-vac and 2W_Si-vac initially contained one and two interstitial H_2O molecules, respectively (see Fig.2). Fig.7a2 and 7b2 shows the bonding character near the defect regions of W_O-vac and W_Si-vac via excess charge density ($\Delta\rho_{excess}$). This quantity was computed using: $\Delta\rho_{excess}=\Delta\rho_{supercell} - \Delta\rho_{Si-O}$ [68, 69, 32, 27]; where, $\Delta\rho_{supercell}$ and $\Delta\rho_{Si-O}$ are charge densities in supercells with and without "water" defects, respectively.

The W_O-vac configuration formed two structures after equilibrating at 300K (Fig.7a1). *First*, the location of prior O^{2-} vacancy reconstructed to form a Si-Si bond, which is indicated with Si1-Si2. Such bonds was recently reported in a 0K-DFT study of α-SiO_2 structure containing

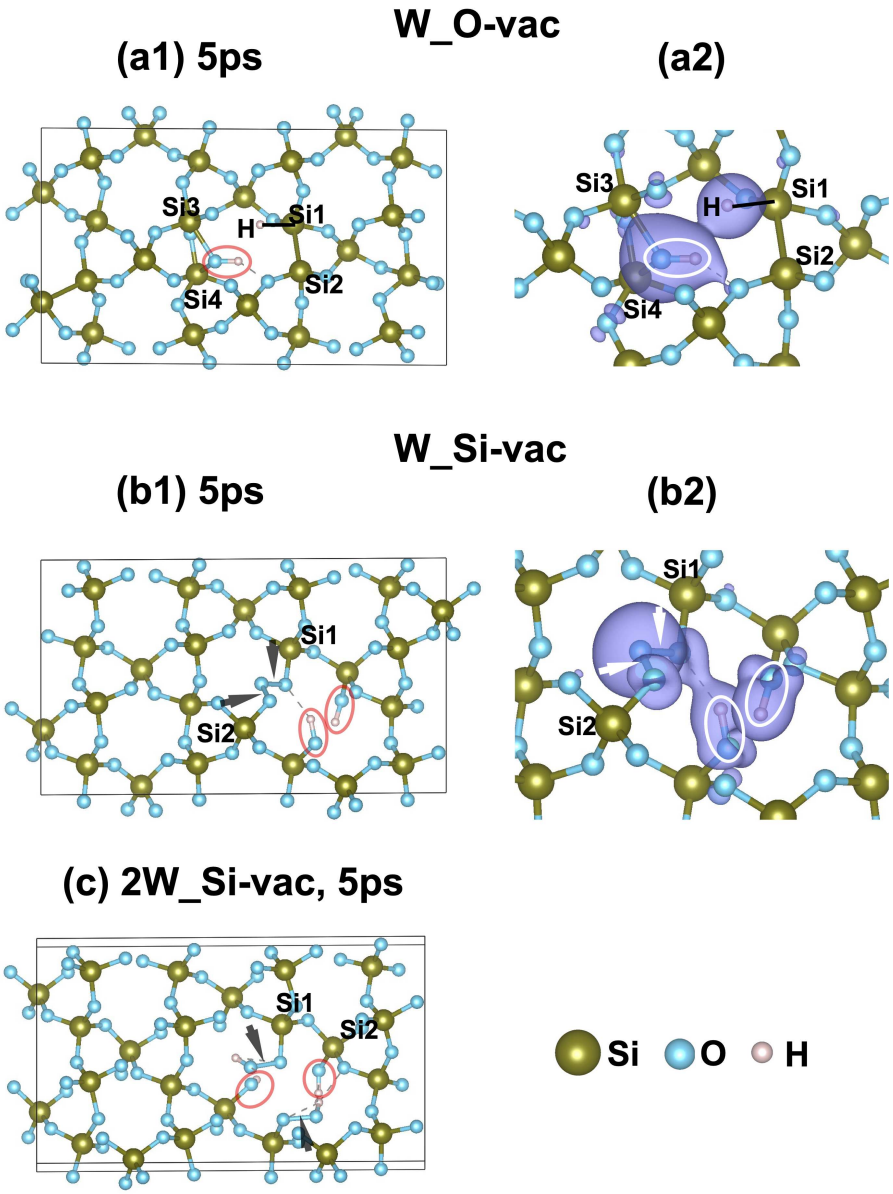

Figure 7: AIMD results at 300K showing equilibrated defects structures and bonding character of (a1)-(a2) W_O-vac and (b1)-(b2) W_Si-vac. (a1) and (b1) depict simulation snapshot at 5ps, while (a2) and (b2) show excess electronic charge density ($\Delta\rho_{excess}$) using blue colored contours. The isocharge contours were drawn using $\Delta\rho$=±0.001Å^{-3}. Dotted lines in (a1) and (b1) indicate hydrogen bonds. These results demonstrate that molecular H_2O dissociates in the presence of O or Si vacancies at 300K.

oxygen vacancy [70]. *Second*, the interstitial H_2O dissociated into OH (marked with an ellipse in Fig.7a1) and a proton (H). The hydroxyl group formed a bridge between Si3 and Si4 atoms, which also increase their coordination from four-fold to five-fold, i.e., they form multi-dentate co-

ordinate complex. The locations of OH and the five-fold coordination of Si atoms are comparable to a Griggs defect [7, 8, 9, 14]. The remaining proton from the prior H_2O was "bound" to Si1 (marked with a black line). Fig.7a2 shows a magnified view of W_O-vac along with $\Delta\rho_{excess}$ contours (colored blue). The excess charge density was localized near the bridging bond Si1-OH-Si2 and Si1-H; meaning, the dissociated remnants of interstitial H_2O are chemically bonded to the surrounding Si atoms. We represent this O^{2-}-mediated H_2O dissociation mechanism as:

$$Griggs\ defect\ formation:\ 2SiO_2 + OH^- \rightarrow O_2Si + OH^- + SiO_2 \tag{4}$$

$$Proton\ localization: SiO_2 + O^{2-}Si(O^{2-}vacancy) + H^+ \rightarrow OSi(H) + SiO_2 \tag{5}$$

In case of Si^{4+} vacancy (e.g.,W_Si-vac configuration; Fig.7b), the H_2O dissociation mechanism differed significantly compared to W_O-vac. W_Si-vac configuration presented in Fig.7b1 shows that the resulting defect is comprised of two terminating hydroxyl groups or Si-OH bonds (marked with ellipses), and a bridging O-O-O bond (marked with arrows) between two Si atoms (indicated as Si1 and Si2). The Si-OH bonds represent another type of Griggs defect [7, 8, 9, 14]. $\Delta\rho_{excess}$ contours presented in Fig.7b2 shows that excess electrons are localized near Si-OH and Si1-O-O-Si2 bonds (marked with arrows), and between on Si-OH one of the O atoms (dotted line in Fig.7b1 and 7b2). These $\Delta\rho_{excess}$ contours indicated that dissociation of a single H_2O near Si^{4+} vacancy forms a chemically interconnected defect structure (somewhat comparable to Fig,7a1). The presence of both Si-O-O-Si and Si-OH bonds are particularly interesting, because, they can potentially result in peroxide-like center, i.e., -O-O-H, within the constrained α-SiO_2 lattice. Such

centers was previously postulated by Jollands et.al. [14]. We have examined this matter using two H_2O molecules near a Si^{4+} vacancy (see 2W_Si-vac in Fig.7e), because it provided extra oxygen and hydrogen. Fig.7c shows the equilibrated 2W_Si-vac configuration, and it comprises the expected Si-OH (marked with ellipses), and two Si-O-O-H bonds with peroxide-like centers (marked with arrows), which are connected to Si1 and Si2 atoms.

Next, we compare and contrast the energetic stability of equilibrated defect configurations in pure α-SiO_2, which are shown in Fig.6 and 7, and those listed in Table.1. Their thermodynamic stability was quantified using enthalpy of formation ($\Delta H_{supercell}$ in eq.1), and the computed values are presented in Fig.8a. In the plot, "W" and "2W" refer to one and two interstitial H_2O, respectively, while "_1" and "_1" indicate two different starting configurations for the same defect (also see Fig.2 and Table.1). Two key observations were noted from Fig.8a: *First*, defects caused by interstitial water molecules (W_in and 2W_in), defects mediated by O^{2-} (W_O-vac) and Si^{4+} (W_Si-vac and 2W_Si-vac), and hydrogarnate (4H_Si-vac_1 and 4H_Si-vac_2) all have negative $\Delta H_{supercell}$ - meaning, all defect configurations are energetically stable. In other words, they can exist (or coexist) in constrained α-SiO_2. *Second*, the defects formed by O^{2-} vacancies and pure α-SiO_2 have comparable energetic stability ($\Delta H^{W\_O-vac}_{supercell} \approx H^{\alpha-quartz}_{supercell}$), and they are more stable than the defects formed by interstitial H_2O and Si^{4+} vacancies. Summarizing their relative energetic stability:

$$\begin{gathered} W\_O-vac > W\_in \approx 2W\_in > \\ 4H\_Si-vac\_1 \approx 4H\_Si-vac\_2 > W\_Si-vac \approx 2W\_Si-vac \end{gathered} \tag{6}$$

The energetic stability indicated via Fig.8a and eq.6 correspond to bulk materials. This is be-

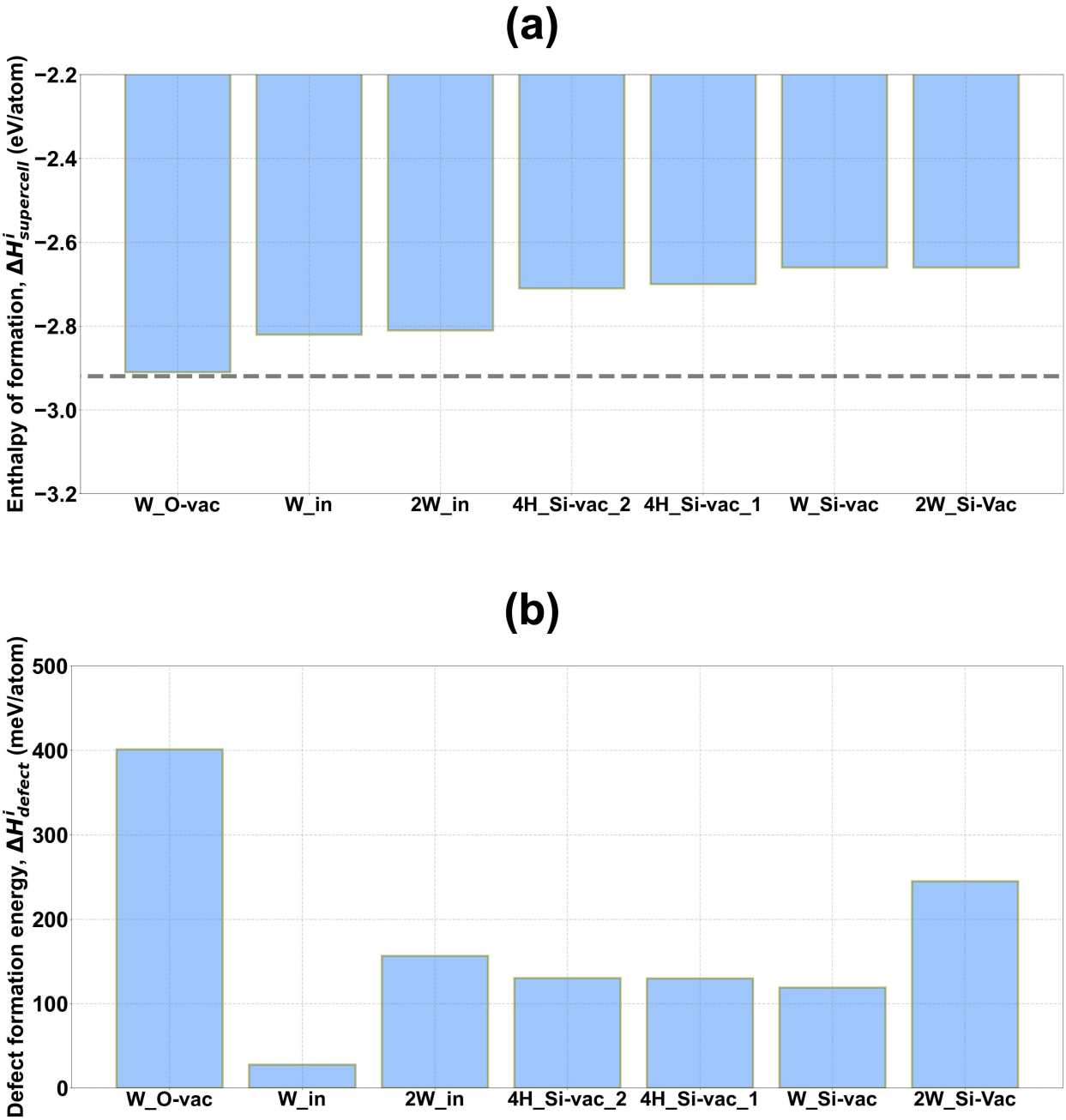

Figure 8: (a) Bar chart comparing the enthalpy of formation ($\Delta H^i_{supercell}$) of different configurations in pure α-quartz. Dotted line shows the energy level for pure α-quartz. (b) Bar chart comparing defect formation energies (ΔH_{defect}) of different configurations.

cause our simulations enforce periodic boundary conditions, and, from a computational point of view, those configurations represent high density of defects within α-SiO_2 (see Table.1, Figs.6

and 7). However, experimental observations indicates that such defects are present in very minor quantities, i.e., parts per million (ppm); meaning, these configurations are embedded inside macroscopic α-SiO_2 crystal [7, 8, 9, 10, 11, 12, 13, 14, 15]. Therefore, it is also useful to compare their defect formation energies to examine their stability relative to the defect-free structure.

For this purpose, we have computed the internal energies of defect configurations by constraining supercell dimensions to that of pristine α-SiO_2 lattice, i.e. volume constraining. Subsequently, configurational energies were compared against strain-free pristine lattice at 300K, using eq.2 (*Section.*2.3). Volume constraints introduces internal strains [68, 24, 71], and increases the overall energy compared to pristine structure. This tendency is depicted in Fig.8b, which shows positive values of defect energies for all configurations; as expected. Interestingly, we find that W_O-Vac has the highest defect energy, which suggests that this defect will introduce more lattice strains compared to other defect-types considered in Fig.8b. Furthermore, several factors will contribute to the higher defect energy of W_O-Vac. It is rather difficult to estimate defect energies for chemically complex systems - as listed Table.1 and depicted in Figs.2-4. We have employed eq.2 to compute defect energies by using pristine α-SiO_2 as reference. A complete estimation may require other reference structures, as well, which may change the relative values. This matter will be further highlighted in *Section.*3.2, where we will examine the effect of impurities on the energetics and structure of water-related defects. However, for defects in pure quartz (without impurities), eq.2 provides a reasonable estimate. Lastly, the presence of W_O-Vac defects due to O^{2-} vacancies is plausible for three reasons: *first*, the presence of such a vacancy is strongly suggested by experimental observations [12]; *second*, charged O^{2-} vacancies are microscopically neutralized by protons that are usually present within the interstitial sites of the quartz lattice [72, 73, 13]; and,

third, impurities can lower the energy of W_O-Vac-like defects. The last point will be investigated in detail in *Section.*3.2.

Fig.8b also showed that interstitial water (W_in) had the lowest defect formation energy at 300K. It is likely that our simpler formulation could have underestimated its value. However, the energy values of W_in (Fig.8) point towards a broader point - the stability of interstitial water in α-SiO_2. In the past, Rosa *et.al.* concluded that α-quartz may contain interstitial water molecules[22]. They utilized a 0K-DFT defect energy formulation that explicitly included energetic contribution from water [22]. However, their 0K-DFT simulations did not incorporate volume constrains. Latter, Jollands *et.al.* examined a comparable structure by employing 0K-DFT and computing the corresponding infrared (IR) spectrum [14], and arrived at a different conclusion. They found that frequencies generated by interstitial water were compatible with experimental observations [14]; meaning, water molecules may exist within the interstitial sites of α-quartz. Therefore, taken together, Jollands *et.al.* 0K-DFT results and our 300K AIMD observations suggest that the presence of interstitial water is *at least thermodynamically feasible*. (Although, kinetics of water absorption, i.e., uptake, may limit the presence of molecular water within α-quartz in detectable quantities [74].) Importantly, these results motivate further theoretical development of defect energy formulations for such covalently bonded materials. Later in Section.3.2, we show that substitutional (Al^{3+}) and interstitial (Li^{+}, Ca^{2+}, and Mg^{2+}) impurities can energetically stabilize interstitial water; even in the presence of a O^{2-} vacancy.

We conclude this section by showing how water-related defects change the local structure of α-SiO_2. Fig.9 plots the radial distribution function (RDF) of different defect configurations, along with control α-SiO_2. Its structure is characterized by distinct peaks in the RDF - a key indicator

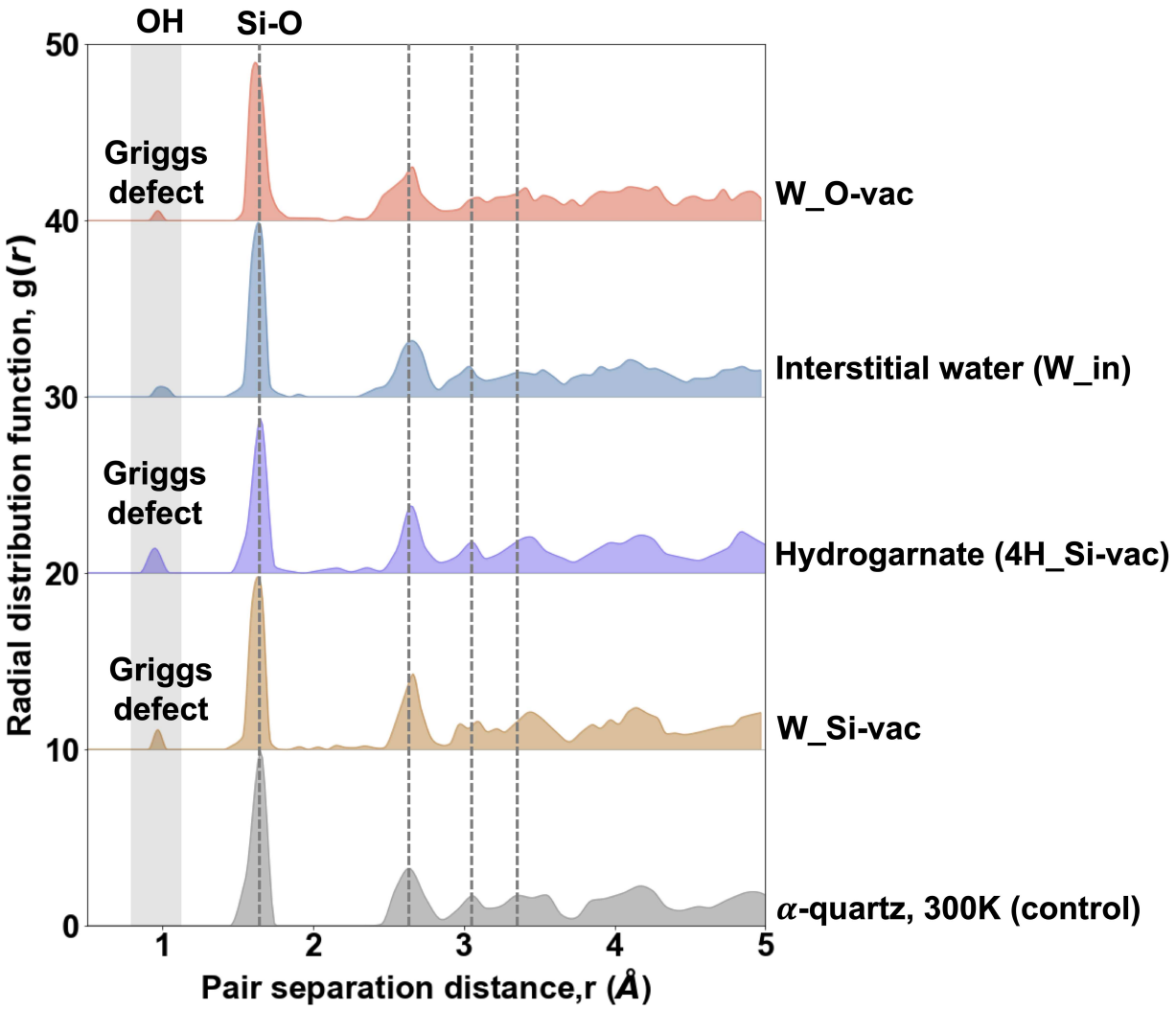

Figure 9: Plots of radial distribution function $g(r)$ show the effect of defects on the structure of α-quartz at 300K. The $g(r)$-pair separation distance plots were obtained from the 5ps snapshots of each configuration. Smallest peaks correspond to Griggs defects and interstitial water, and they are indicated with a shaded column. These results show that water-related defects discernible affect the higher order coordination shells in α-quartz.

of crystalline structure [75, 67, 42, 76, 77, 27]. For example, Fig.9 shows peaks corresponding to 1^{st}, 2^{nd}, 3^{rd} and 4^{th} coordination shells α-SiO_2 via dotted lines. A key difference between defect configurations and control α-SiO_2 is the presence of a small peaks within 0.96-0.98Å: They are related to either Griggs defect (W_O-Vac, 4H_Si-vac, and W_S-vac) or interstitial water (W_in). Other prominent peak positions of defect configurations are comparable to 1^{st} and 2^{nd}

order coordination shells, which correlate to Si-O, S-H and O-H (hydrogen bonding between H and O) bond lengths. However, defect configuration peak positions start to deviate from the 3^{rd} coordination shell of α-SiO_2 (compare with 4H_Si-vac), and are noticeably different for higher order coordination shells. For example, the lower-energy W_O-Vac and W_in configurations do not manifest well-defined, higher order peaks compared to α-SiO_2. These differences suggest that water-related defects limit long range ordering, but retain short-range ordering (corresponding to the 1^{st} and 2^{nd} order coordination shells). This reduction in long-range structural ordering can be further affected by substitutional and interstitial species that have larger atomic radii than Si, O and H. Consequently, we have probed the effect of larger atoms on the energetics and structure of water-related defect configurations in *Section.*3.2.

Summarizing, our AIMD examination of "pure" α-SiO_2 revealed that defects produced by O^{2-} vacancy was energetically comparable to the pristine lattice, e.g., W_O-vac in Fig.8a. Furthermore, O^{2-} vacancy formation requires a smaller energetic penalty than Si^{4+} [78, 70], because, notionally, the former requires breaking two Si-O bonds while the latter involves four Si-O bonds. However, simple O^{2-} vacancy without substitution may lead to a build-up of strain that, after formation, would decrease the overall stability of lattice when relative to α-quartz, at least compared to other defects. In sum, they imply that O^{2-} vacancy are more prevalent than Si^{4+}, and, consequently, O^{2-} vacancies will more likely contribute towards forming water-related defects in α-quartz. Next, we consider the effect of impurities on defect energetics.

3.2. Effect of substitutional and interstitial species on water-related defects at 300K

For this purpose, we substituted Si^{4+} with Al^{3+} ions, and added appropriate number of charge compensating Li^{+}, Ca^{2+} and Mg^{2+} to the interstitial sites; specifically, Ca^{2+} and Mg^{2+} was added to prior Al^{3+} and Li^{+} containing α-SiO_2 (see Fig.3 and 4, and Table.1). Furthermore, we will focus on examining their effects in the presence of an O^{2-} vacancy. This choice of combining three kinds of point defects,i.e., O^{2-} vacancy, substitutional, and interstitial, was guided by findings reported Stenina [12]. By employing TEM of natural quartz, they suggested that trivalent cations in conjunction with O^{2-} vacancies, and monovalent and divalent ions can stabilize "water" (in interstitial or OH form) within α-SiO_2 lattice (see Fig.12 in [12]). Therefore, 300K-AIMD equilibration of configurations involving impurity atoms, presented in Fig.3 and 4, will provide energetic and structural insights that could not be obtained from TEM, only.

The bar plot presented in Fig.10a shows the effect of chemistry on the enthalpy of formation ($\Delta H_{supercell}$) of different defect configurations. All configurations had negative $\Delta H_{supercell}$ - meaning, they are thermodynamically stable at 300K. To better understand their relative energetic stability Fig.10a was divided into two categories: One comparing structures containing Al^{3+} substitutions and Li^{+} interstitials (AlLi-based), and the other after adding Ca^{2+} or Mg^{2+} interstitials to energetically stable AlLi-based configurations. The AlLi-based structures also included "2Al2Li" and "AlLi" configurations that were without O^{2-} vacancy, and a structure without Al^{3+} containing two Li^{+} interstitials and O^{2-} vacancy, i.e., 2Li_O-vac. We will first discuss the energetics and structure of AlLi-based configurations.

Among the AlLi-based structures, AlLi_O-vac was energetically most stable and was followed by 2Al2Li. Interestingly, our results show that AlLi_O-vac and 2A2Li_O-vac was more stable than

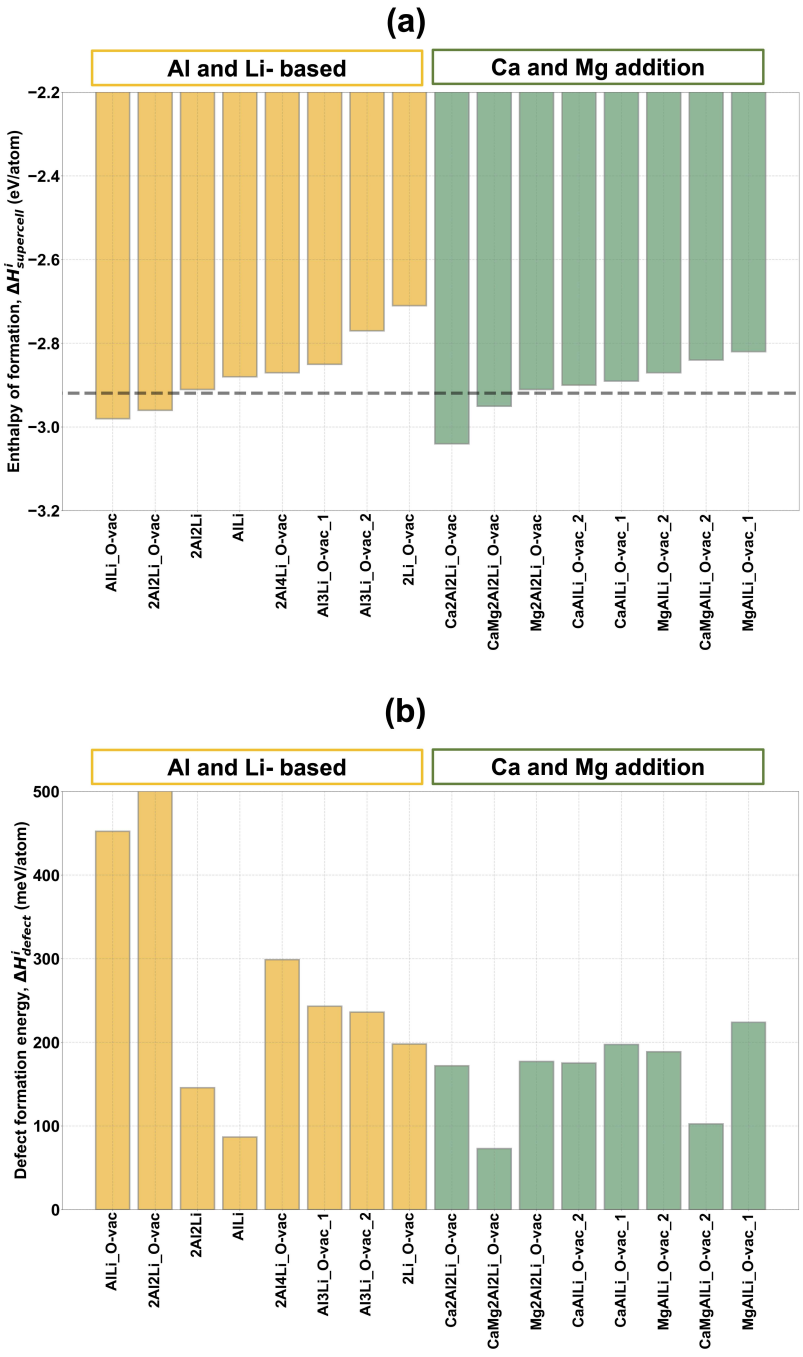

Figure 10: (a) Bar chart showing the effect of substitutional (Al) and interstitial (Li, Mg, Ca) atoms on the enthalpy of formation ($\Delta H^i_{supercell}$). "_O-vac" denotes the presence an O vacancy in the initial structure. Dotted line shows the energy level for pure α-quartz. The defects structures containing larger Ca interstitial ions appears to be energetically more favorable than the smaller Li and Mg. (b) Bar chart comparing the effect of substitutional (Al) and interstitial (Li, Mg, Ca) atoms on the defect formation energy (ΔH^i_{defect}).

pristine α-SiO_2 (control) at 300K, i.e., $\Delta H^{AlLi\_O-vac}_{supercell} < \Delta H^{\alpha-quartz}_{supercell}$ and $\Delta H^{2Al2Li\_O-vac}_{supercell} < \Delta H^{\alpha-quartz}_{supercell}$, while 2Al2Li was nominally comparable to the control specimen, i.e. $\Delta H^{2Al2Li}_{supercell} \approx H^{\alpha-quartz}_{supercell}$. Note, 2Li_O-vac had the lowest stability in this category. Taken together, these results underscore the combined influence of substitutional Al^{3+}, interstitial Li^{+}, and vacant O^{2-} sites on the thermodynamically stabilizing water defects in α-SiO_2. The relative stability of AlLi-based configurations are summarized below:

$$\begin{aligned} &AlLi\_O - vac > 2A2Li\_O - vac > 2A2Li > \\ &AlLi \approx 2Al4Li\_O - vac \approx Al3Li\_O - vac\_1 > \\ &Al3Li\_O - vac\_2 > 2Li\_O - vac \end{aligned} \tag{7}$$

We have also examined the effect of substitutional (Al^{3+}) and interstitial (Li^{+}, Ca^{2+}, and Mg^{2+}) impurities on defect formation energies by using eq.1a (see Fig.10b). As mentioned earlier, it is difficult to derive or postulate a generalized expression for computing defect formation energies, because of the diversity of chemical species considered in this study. Such an expression may involve energies of naturally occurring oxides and hydrides of Al, Li, Ca and Mg as references, together with formation energies of charged vacancies, i.e. O^{2-} and Si^{4+}. This will increase computational complexity, especially for AIMD, because that would require us to incorporate both long ranged van der Waals interactions and appropriate Hubbard constants [79, 53]. Such computationally intensive study is beyond the scope of current investigation, and is the subject of a separate effort.

Notwithstanding, application of our simple formulation (eq.2), and resulting plot depicted in

Fig.10b, provided a key insight into effect of impurities on defects containing O^{2-} vacancy. Fig.10b show that defects with low impurity content and O^{2-} vacancy have a higher ΔH^{i}_{defect} values, e.g., AlLi_O-vac and 2Al2Li_O-vac. However, increasing impurity content and impurity type (Ca and Mg) reduces the defect formation energies. It implies that such additions reduce internal strains, and, by extension, strain energy. Such reduction may manifest as change in the local structure, e.g. rupture or distortion of bonds between SiO_2 tetrahedra, reduction in ordering, and the like. Structures of water-related defects with impurities are described next.

Fig.11 presents the equilibrated structures of the first three stable configurations in eq.7, i.e., AlLi_O-vac (Fig.11a), 2A2Li_O-vac (Fig.11b), and 2A2Li (Fig.11c); and their corresponding RDFs (Fig.11d). The structures of AlLi_O-vac and 2A2Li_O-vac show that prior O^{2-} vacancy facilitates in the dissociation of interstitial H_2O inside the α-SiO_2 lattice, which is comparable to the "pure" defect configuration presented in Fig.7a1, i.e., W_O-vac. In case of AlLi_O-vac, the two protons are located next to Si atoms (Si1 and Si2) that were located next to the prior O^{2-} vacancy (see Fig.2a), and the oxygen atom in H_2O - marked O1 - was "consumed" by the surrounding cage by forming an bridge between the substitutional-Al and Si3. Specifically, this atom shifted the prior oxygen atom - marked O2 -, that previously bridged Si3 and Al, to a new position next to Si4. (Also worth noting that equilibration formed a bond between Si1 and Si2). In other words, H_2O dissociation structurally and chemically altered the neighborhood of impurities in AlLi_O-vac configuration. Such impurity-centered alterations were also evident in 2A2Li_O-vac, but with two key differences compared to AlLi_O-vac. In 2A2Li_O-vac, H_2O dissociated into a hydroxyl group (attached to Si1) or Griggs defect, and a proton next to another Si atom (marked Si2). In some locations, several interconnecting M(Si or Al)-O-Si bonds were missing - indicated using

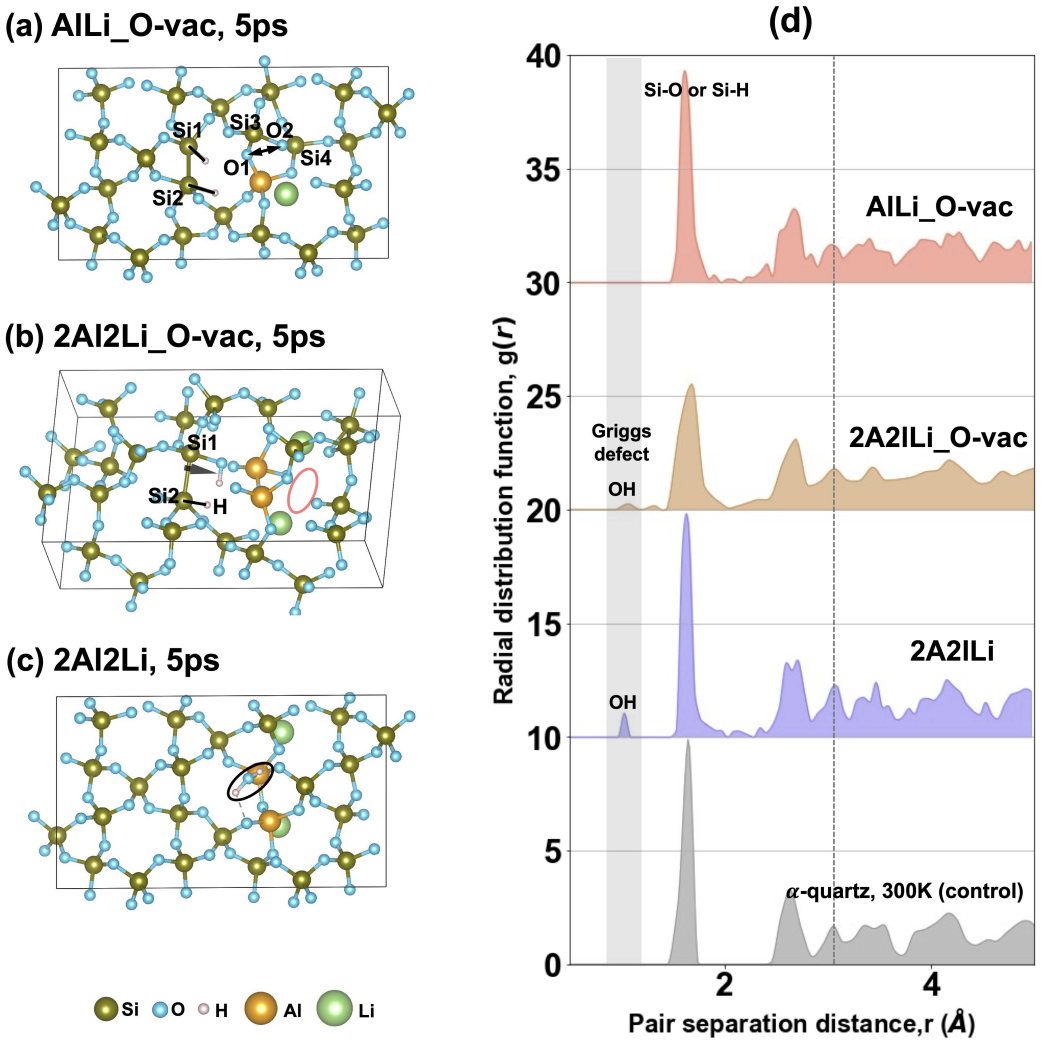

Figure 11: Equilibrated structures of water containing α-quartz, where Si is substitute by trivalent-Al and monovalent-Li located at the interstitial sites. AIMD snapshots at 5ps of (a) AlLi_O-vac with O vacancy, (b) 2Al2Li_O-vac with O vacancy at and (c) 2Al2Li without O vacancy at 300K. Bonds between the interstitial Li^+ and its surrounding are not shown in order to highlight their interstitial nature. (d) compares the radial distribution function of the three defect configurations. The dotted line in panel "d" shows third order coordination shell in pure α-quartz at 300K.

an ellipse. In stark contrast to both configurations, H_2O in 2Al2Li (with O^{2-} vacancy) remained undissociated, where the molecule was lodged next to a Si lattice site- comparable to W_in. Furthermore, the Si-O-Si bonds within α-SiO_2 lattice remained unbroken, albeit distorted compared to the pristine structure at 300K.

The structure of the three configurations, AlLi_O-vac, 2Al2Li_O-vac , and 2Al2Li, were also

examined using RDFs. Plots presented in Fig.11d compares their RDFs with control α-SiO_2. AlLi_O-vac did not show an OH peak at 0.96-0.98Å (shaded region in Fig.11d), due to the absence of either OH or H_2O in its configuration (see Fig.11a). However, 2A2Li_O-vac , and 2A2Li manifested those peaks because they contained a Griggs defect and interstitial H_2O, respectively. RDFs of AlLi_O-vac and 2A2Li_O-vac were discernibly different from control α-SiO_2 after ~3.1Å (marked with dotted line). For example, AlLi_O-vac multiple peaks, while they were barely visible in 2A2Li_O-vac. These differences point towards local deviations in the structure of Si-O-Si cages. Interestingly, the peaks in 2Al2Li were somewhat comparable to α-SiO_2; although peak slitting was noted in the second coordination shell of 2Al2Li. Taken together, these results reveal that dissociation of H_2O disrupts the local coordination and structure of α-SiO_2. Comparison with W_O-vac (see Fig.9) shows that such structural disruptions are further exacerbated by the presence of substitutional and interstitial point defects.

Next, using eq.7 as guide, we incorporated interstitial Ca^{2+} and Mg^{2+} (both individually and together) in the initial structures of AlLi_O-vac and 2A2Li_O-vac. Enthalpy of the equilibrated structures are shown in Fig.10a (green colored bars). The relative stability of Ca^{2+}/Mg^{2+}-incorporated AlLi-based configurations were:

$$\begin{aligned} Ca2Al2Li\_O-vac > CaMg2A2Li\_O-vac > Mg2A2Li\_O-vac > \\ CaAlLi\_O-vac\_2 > CaAlLi\_O-vac\_1 > \\ MgAlLi\_O-vac\_2 > CaMgAlLi\_O-vac\_2 > MgAlLi\_O-vac\_1 \end{aligned} \tag{8}$$

Ca2Al2Li_O-vac is energetically the most stable structure at 300K among all the configurations ex-

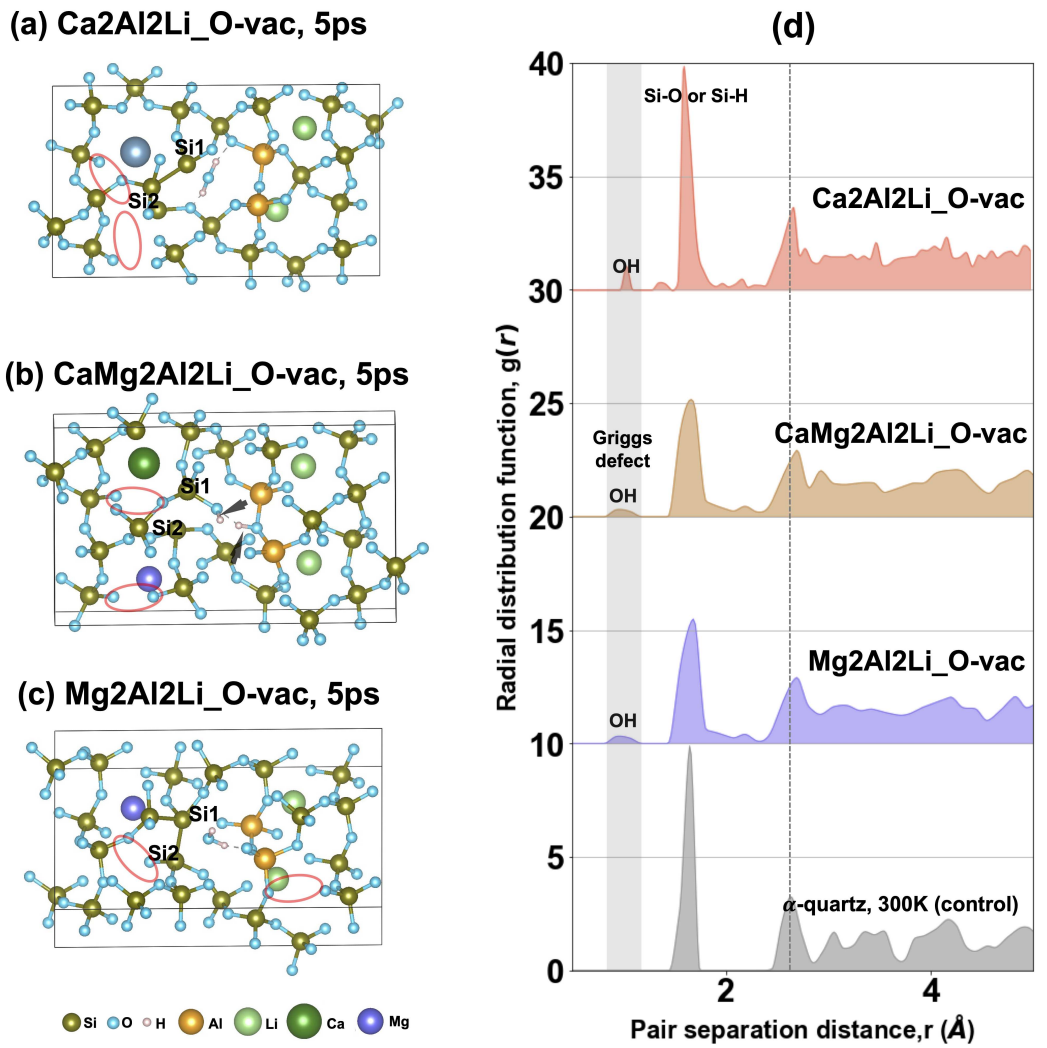

Figure 12: AIMD snapshot at 5ps compares the equilibrated structure of (a) Ca2Al2Li_O-vac , (b) CaMg2Al2Li_O-vac, and (c) Mg2Al2Li_O-vac at 300K. (d) compares the radial distribution function of the three defect configurations. Bonds between the interstitial Ca^{2+}, Mg^{2+} and Li^{+}, and their surrounding are not shown in order to highlight their interstitial nature. The dotted lines in panel "d" show second order coordination shell in pure α-quartz at 300K. The lack of distinct peaks corresponding to the higher order coordination shells in Ca2Al2Li_O-vac, CaMg2Al2Li_O-vac and Mg2Al2Li_O-vac indicates loss of long-range order.

amined in this work; it is more stable than AlLi_O-vac and 2A2Li_O-vac, and pristine α-SiO_2 (dotted line in Fig.10a). Broadly, we find that incorporation of interstitial Ca^{2+} tends to form energetically more stable defect configurations compared to Mg^{2+} and Li^{2+} alone. We have further examined the structures of three most stable configurations in eq.8a. Fig.11a-c shows the structures of

Ca2Al2Li_O-vac, CaMg2A2Li_O-vac, and Mg2A2Li_O-vac, respectively, and, Fig.11d compares their RDFs with control. CaMg2A2Li_O-vac contained Griggs defect, while CaMg2A2Li_O-vac and Mg2A2Li_O-vac retained interstitial water. The latter two structures - shown in Fig.12a and 12b - are comparable to the "aqua complex" defect that was proposed by Stenina using TEM observation of natural quartz [12]. That study proposed that interstitial water is stabilized by the presence of substitutional and interstitial ions, and oxygen vacancies: CaMg2A2Li_O-vac and Mg2A2Li_O-vac satisfies all these conditions. Therefore, it is not surprising that they are more energetically favorable than W_in (Fig.8 and Fig.10a), and among the more stable within the configurations employed in this study.

Furthermore, a careful examination of the three substitutional and interstitial defect structures show that SiO_4^{4-} tetrahedra around the substitutions are disconnected from the adjoining tetrahedron. Examples of such disconnections are indicated using ellipses in Fig.11a-c. Another instance of "broken" bonds was seen in CaMg2A2Li_O-vac: the two Si atoms (Si1 and Si2), with a prior O^{2-} vacancy, did not form a bond after 5ps at 300K. These structural disruptions - specifically in case of SiO_4 tetrahedra - is indicative of ordering till first or second nearest neighbors, but loose structural integrity at higher order coordination shells. This matter is highlighted in the RDFs presented in Fig.12d. Here, RDFs of three structures were substantially different from the control specimen after second nearest neighbor shell (see dotted line). Ca2Al2Li_O-vac tends to show several high order peaks with substantially differing positions compared to control α-SiO_2. On the other hand, such peaks in CaMg2A2Li_O-vac, and Mg2A2Li_O-vac were barely visible compared to the background. Taken together, these RDFs reveal that incorporation of interstitial and substitutional point defects, along with water (dissociated or not), in α-SiO_2 results in local loss

of long-range crystalline ordering of the host lattice. Stenina showed that such water defects can produce local amorphization within quartz [12], and our AIMD results - presented in Figs.10a and 12 - rationalizes their observation on the basis of energetics, structure and chemistry.

4. Discussion

The major finding of this work is that water can exist within α-SiO_2 lattice in multiple, energetically favorable defect configurations (Figs.8a and 10a). In fact such water-related defect configurations are further stabilized in the presence of substitutional (e.g., Al^{3+} replacing Si^{4+}) and interstitial (e.g., Ca^{2+}, Mg^{2+} and Li^{+}) point defects. Table.2 list all the α-SiO_2-based configurations examined in this study (also see Table.1), and the corresponding water defects. Prior to this study, these structures were posited based on infra-red spectroscopy and transmission electron microscopy observations, but there were limited studies on gaining physics-based understanding of water-related defect structures [7, 8, 9, 10, 15, 18, 12, 13, 20, 19, 21, 22, 14].

Broadly, five categories of water defects were identified in our simulations that can exist volume-constrained α-SiO_2 at 300K: (I) molecular water present at the interstitial sites: (II) hydroxyl (OH^{-}) group attached directly to individual Si and as a bridge between Si atoms (Figs.6), i.e., Griggs defect [7, 8, 9, 14]; (III) "free" protons (H^{+}) located near Si lattice sites (Figs.6 and 11); and (IV) -O-O-H peroxide-like bonds attached to Si atoms (Figs.6); and (V) -O-O-O- connecting two Si atoms (Figs.6). Substitutional and interstitial ions and oxygen vacancy stabilizes molecular water within α-SiO_2 lattice - defect (I). We also found that O^{2-} or Si^{4+} vacancies facilitated the dissociation of molecular water and helped in the formation of defects (II)-(V), e.g., see Figs.6b, 7, 11a-b, and 12a-b. Defects formed only by O2- vacancies with limited further substi-

Table 2: List of defects found in each configuration after equilibration at 300K. Here, H_2O indicates interstitial water, OH^- Griggs defect, and H^+ detached proton. Unless indicated otherwise most configurations contained one interstitial water molecule in their initial configuration.

Configuration	**H_2O dissociation**	**Defect type** [a]
W_ in	N	(1) H_2O (Interstitial)
2W_ in[b]	N	(2) H_2O (Interstitial)
W_ in_O-vac	Y	(1) OH^- (Griggs), and (1) H^+ (Proton)
W_ in_Si-vac	Y	(2) OH^- (Griggs), and (1) O-O-O (O bridge)
2W_ in_Si-vac[b]	Y	(2) OH^- (Griggs), and (2) O-O-H (peroxide-like)
4H_Si-vac_1[c]	Y	(4) OH^- (Griggs)
4H_Si-vac_2[c]	Y	(4) OH^- (Griggs)
AlLi	N	(1) H_2O (Interstitial)
AlLi_O-vac	Y	(2) H^+ (Proton), and O^{2-} was consumed within the surrounding cages formed by Si-O-Si and Si-O-Al
2Al2Li	N	(1) H_2O (Interstitial)
2Al2Li_O-vac	N	(1) H_2O (Interstitial)
2Al4Li_O-vac	Y	(1) OH^- (Griggs), and (1) H^+ (Proton)
Al3Li_O-vac_1	Y	(1) OH^- (Griggs), and (1) H^+ (Proton)
Al3Li_O-vac_2	Y	(1) OH^- (Griggs), and (1) H^+ (Proton)
2Li_O-vac	N	(1) H_2O (Interstitial)
Ca2Al2Li_O-vac	N	(1) H_2O (Interstitial)
CaAlLi_O-vac_1	N	(1) H_2O (Interstitial)
CaAlLi_O-vac_2	Y	(1) OH^- (Griggs), and (1) H^+ (Proton)
Mg2Al2Li_O-vac	N	(1) H_2O (Interstitial)
MgAlLi_O-vac_1	N	(1) H_2O (Interstitial)
MgAlLi_O-vac_2	Y	(1) OH^- (Griggs), and (1) H^+ (Proton)
CaMg2Al2Li_O-vac	Y	(2) OH^- (Griggs)
CaMgAlLi_O-vac_2	Y	(1) OH^- (Griggs), and (1) H^+ (Proton)

[a] Number of defects are indicated inside the parenthesis. [b] Contained two water molecules in the initial configuration. [c] Interstitial water was not present in the initial configuration.

tutions led to large energetic differences from α-quartz, indicating lattice strains. This is despite their overall lowest energy of formation. Such vacancies, then, may be preferentially deformed or reacted with other defect types. Using Table.2, the quantified the number frequency of five defect types, and their relative fractions are plotted in Fig.13. It shows that Griggs defect (i.e., OH^- group) had the highest fraction (~50%), followed by interstitial water and protons at comparable concentrations (~20%). Comparatively, peroxide-like and O-bridging fractions were lower by an order of magnitude. Thus, our simulations provide a subjective guideline on the relative abundance

of water-related defects in quartz-based minerals; albeit limited by the number of configurations examined in this study.

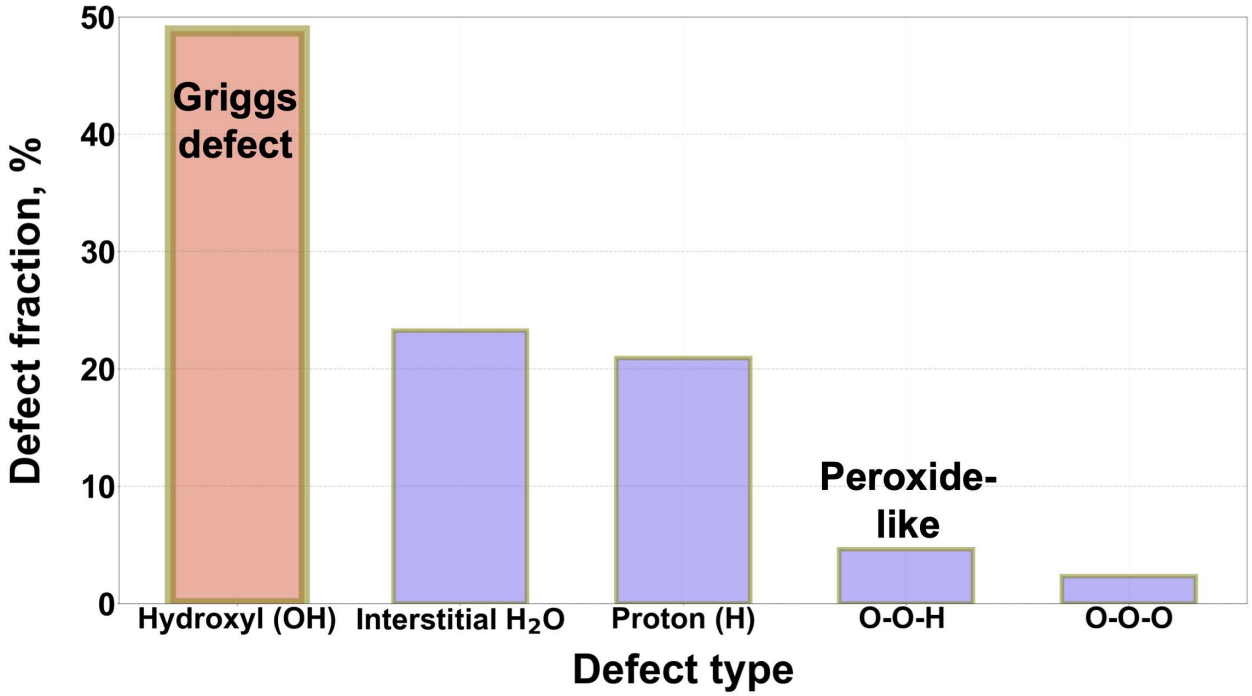

Figure 13: Bar chart showing the frequency distribution of water-related defects determined from all the configurations examined in this study.

The high fraction of OH-based Griggs defects - in Fig.13 - are consistent with their relative abundance observed in experimental observations [11, 13, 14]. They are typically detected using infrared-based (IR) spectroscopy, where the measured spectra is proportional to the sampling volume. Therefore, higher fractions of hydroxyl groups will manifest as a prominent peak, and may "hide" signals from other defects, i.e., -O-O-H and -O-O-O-. Signals emanating from OH bond vibrations in molecular water can also add to peaks corresponding to Griggs defects. Therefore, AIMD simulations carried out relevant temperatures (compared to 0K-DFT) and pressures can complement experimental observations by uncovering energetically favorably, plausible water-related defects.

Also worth noting are the presence of protons within α-SiO_2 lattice (e.g., see Figs.7a and 11a), which has two implications in the context of water dissociation. *First*, protons can diffuse through the host lattice at higher temperatures [72, 73], and locally neutralize any charge balance without hindering structural changes, e.g. chemical reaction events. An example of such an event is the dissociation of molecular H_2O in the presence of charge centers, like O^{2-} and Si^{4+} ion vacancies. Protons can diffuse through the host lattice high temperatures and locally neutralize. *Second*, recently it was reported that molecular hydrogen (H_2) can exist in earth's iron-rich mantle [80]. It is thought that H_2 production is facilitated by the dissociation of water molecules that are in contact with iron-rich minerals [80]. Vacancy mediated water dissociation could be a potential mechanism for explaining such naturally occurring process. However, this mechanism remains to be interrogated in as a function of thermodynamic variables.

This study opens door for studying the impact of water on the behavior of silicate anhydrous minerals, particularly quartz, at the atomistic level. The amount of water and the nature of defects in silicate rocks, i.e., polycrystalline assemblages of silicate minerals, has been correlated to a wide range of behaviors. At low temperatures and stresses, these include water-weakening of silicate rocks via stress corrosion and fatigue properties [81, 82, 83, 84], rates of chemical weathering , and the brittleness of the rock [85, 86, 87, 88, 89]. Deeper in the crust, water content allows ductile deformation to begin at lower temperatures and stresses than truly dry materials [90, 91, 92, 93] . Water content is also related to a decrease in melt temperatures, helping to drive the movement of refractory and volatile elements up from depth [91]. Additionally, the presence of water in defects has been posited as a possible source of water throughout its body early in Earth's history and in extraterrestrial bodies [94, 95, 96, 97].

While our simulations were performed at nominally 300 K, they are already indicative of some of the mechanisms causing these behaviors. We observed that all water-related defects are thermodynamically stable – all are predicted to be able to form as observed. We have outlined how they can be stable and their relative stability, which provides confirmation of the thermodynamic possibility of nominally anhydrous minerals bearing water early in Earth's history. Water in oxygen vacancies, the presence of interstitial water, oxygen vacancies with Li and Al replacement, and all divalent replacements lead to the disruption of third order and higher coordination. By creating a far-field amorphous region, these water-related defects enhance the onset of both stress concentrations and possibly the onset of ductile deformation at 300 K. Similarly, this loss of far-field structure may allow more rapid dissolution/precipitation kinetics as observed in other anhydrous silicate minerals [98, 99].

5. Summary

Ab initio molecular dynamics (AIMD) simulations were performed at 300K to examine the stability of water molecules inside volume-constrained α-quartz. Several configurations were examined by incorporating point defects within equilibrated α-quartz lattice maintained at fixed volume. Specifically, we examined the stability of an interstitial water molecule in the presence of O and Si vacancies, substitutional Al, and interstitial Ca, Mg and Li ions. These configurations were characterized computing their enthalpy of formation, analyzing their effects on the neighboring structure and frequency of occurrence. Our main findings are as follows:

1. Energetic considerations indicated that oxygen vacancies, substitutional Al, and interstitial Ca, Mg and Li ions permits the presence of molecular water within the interstitial sites of

volume-constrained-α-quartz.

2. Interstitial water also demonstrated a strong tendency to dissociate in the presence of O and Si vacancies. Four types of dissociation products was uncovered from our simulations: hydroxyl (OH^-) or Griggs defects, proton (H^+), peroxide-like (-O-O-H), and bridging-O between SiO_4^{4-} tetrahedra.

3. Griggs defects were most prevalent among all the volume-constrained configurations examined in this study. It formed in substantially greater quantities than interstitial water and protons, while -O-O-H and bridging-O were minimally present.

4. Addition of Ca, Mg and Li to the interstitial sites substantially distorted the host α-SiO_2 lattice. In the extreme case, it resulted in the disruption of long range ordering of the host structure, but retained short-to-medium range ordering to the second nearest neighbor. Notwithstanding, these substitutions yielded energetically favorable water-related defects.

Acknowledgments

DC acknowledges funding from NSF DMR-2333630, and AJR is thankful for NMT's faculty start-up funding. DC also acknowledges computation time on the Alpine High Performance Computing resource at the University of Colorado Boulder. Alpine is jointly funded by the University of Colorado Boulder, the University of Colorado Anschutz, Colorado State University, and the National Science Foundation (award # 2201538).

Author contributions

Deep Choudhuri: Conceptualization (equal); Writing – review & editing (equal); Project administration (equal); Funding acquisition; Methodology; Resources; Visualization. **Alex J. Rinehart**: Conceptualization (equal); Writing – review & editing (equal); Funding acquisition.

Appendix A. Structural properties obtained from 0K-DFT of α-quartz

Table .3: Summary of structural properties of α-quartz obtained from energy minimization.

Structural parameters	**This work**	**Literature (DFT)***	**Experimental**^{d}
a (Å)	5.02	4.98^a, 5.01^b	4.92
c (Å)	5.51	5.46^a, 5.51^b, 5.55^c	5.41
Si-O (Å)	1.63	1.63^a, 1.63^c	1.61
∠Si-O-Si (°)	147.03	143.3^a, 147.9^c	143.7
∠O-Si-O (°)	108.3-110.5	108.1-110.6^a	108.8 - 110.5

* Uses hexagonal lattice. ^{a} [22]. ^{b} [14]. ^{c} [62]. ^{d} [60].

Table..3 shows that our DFT-computed structural parameters are in reasonable agreement with extant DFT studies that used GGA-PBE approach [22, 14, 62], and experimental data [60].

Appendix B. Derivation of Equation No.1 in *Section*.2.3

We start with the classical thermodynamics definition for enthalpy [66]:

$$H_i = U_i + P_i^{int} V_i, \tag{9}$$

where, H_i is enthalpy, U_i internal energy, P_i^{int} internal pressure and V_i volume of the system corresponding to the i^{th} configuration after they are equilibrated at 300K (e.g., see Figs.6, 7, 11 and

12). Taking differential of eq.9 gives,

$$dH_i = dU_i + P_i^{int} dV_i + V_i dP_i^{int}. \tag{10}$$

AIMD simulations were performed using the NVT ensemble (i.e., dV_i=0), where supercell, corresponding to the i^{th} configuration, *was constrained to the equilibrated volume of α-quartz supercell*; meaning, $V_i = V^{\alpha}$. These simulations also calculate the *external pressure* (P_i^{ext}) at each time step, and one can assume the following equivalence at equilibrium (e.g. see Fig.5 in *Section*.2.3): P_i^{int} + P_i^{ext} = 0. Taken together, eq.10 can be rewritten:

$$dH_i = dU_i - V^{\alpha} dP_i^{ext}. \tag{11}$$

Integrating eq.11 and taking average over several time steps gives the change in enthalpy of the i^{th} configuration:

$$\langle \Delta H_i \rangle = \langle \Delta U_i \rangle - V^{\alpha}(\langle P_i^{ext} \rangle - \langle P_{\alpha}^{ext} \rangle), \tag{12}$$

where, $\langle ... \rangle$ is the ensemble average, $\langle \Delta U_i \rangle$ is essentially the Hamiltonian that is obtained by adding the AIMD-computed potential ($\langle \mathcal{V} \rangle$) and kinetic ($\langle \mathcal{KE} \rangle$) energies, i.e., $\langle \mathcal{U} \rangle = \langle \mathcal{V} \rangle + \langle \mathcal{KE} \rangle$ [41], $\langle P_i^{ext} \rangle$ is the average external pressure on the supercell of the i^{th} configuration, and $\langle P_{\alpha}^{ext} \rangle$ the reference external pressure obtained after equilibrating α-quartz at 300K. We computed that $\langle P_i^{ext} \rangle \in$[-3.7,5.6] and $\langle P_{\alpha}^{ext} \rangle$=0.01 (units in GPa).

Next, we *define* the heat of formation of an i^{th} configuration supercell as,

$$\Delta H^{i}_{supercell} = \frac{1}{N_{Total}}\langle \Delta H_i \rangle - \sum_{k=Si,O,H,Al,Li,Ca,Mg} \frac{n_k}{N_{Total}}\langle \Delta H_k \rangle. \quad (13)$$

Eq.13 essentially calculates that change in energy that results after forming the structure corresponding to the i^{th} configuration (product) by "bringing together" relevant k elements (reactants): Eq.13 is based on a well-known formulation used for quantifying reaction energetics $\Delta H = \Delta H_{product} - \sum \Delta H^{k}_{reactants}$ [100]. Next, substituting eq.12 in eq.13 gives,

$$\Delta H^{i}_{supercell} = \frac{1}{N_{Total}}[(\langle \mathcal{V} \rangle + \langle \mathcal{KE} \rangle) - V^{\alpha}(\langle P^{ext}_{i} \rangle - \langle P^{ext}_{\alpha} \rangle)] - \sum_{k=Si,O,H,Al,Li,Ca,Mg} \frac{n_k}{N_{Total}}\langle \Delta H_k \rangle, \quad (14)$$

where, N_{Total} is the total number of atoms present in the supercell cell, n_k number of atoms of k^{th} element, and $\langle H_k \rangle$ is enthalpy of the k element in its stable structure at 300K. The dimensions of supercells containing the pure elements were systematically adjusted to a nominal external pressure of ~0GPa. However, we have applied eq.11 to account even at pressures for computing their enthalpy, e.g., P^{ext}_{i}∈[-0.5,0.08] (GPa units). Notionally, eq.14 describes the energy required to form the supercell structures by bringing together all relevant elements that are at equilibrium under nominally ambient conditions, i.e., 300K and ~0GPa (1atm = 1.01325×10^{-5} GPa).

References

[1] R. Musat, J. P. Renault, M. Candelaresi, D. J. Palmer, S. Le Caër, R. Righini, S. Pommeret, Finite size effects on hydrogen bonds in confined water, Angewandte Chemie International Edition 47 (42) (2008) 8033–8035.

[2] I. C. Bourg, C. I. Steefel, Molecular dynamics simulations of water structure and diffusion in silica nanopores, The Journal of Physical Chemistry C 116 (21) (2012) 11556–11564.

[3] M. Collin, S. Gin, B. Dazas, T. Mahadevan, J. Du, I. C. Bourg, Molecular dynamics simulations of water structure and diffusion in a 1 nm diameter silica nanopore as a function of surface charge and alkali metal counterion identity, The Journal of Physical Chemistry C 122 (31) (2018) 17764–17776.

[4] A. W. Knight, N. G. Kalugin, E. Coker, A. G. Ilgen, Water properties under nano-scale confinement, Scientific reports 9 (1) (2019) 8246.

[5] T. Takei, K. Mukasa, M. Kofuji, M. Fuji, T. Watanabe, M. Chikazawa, T. Kanazawa, Changes in density and surface tension of water in silica pores, Colloid and Polymer Science 278 (2000) 475–480.

[6] S. Senapati, A. Chandra, Dielectric constant of water confined in a nanocavity, The Journal of Physical Chemistry B 105 (22) (2001) 5106–5109.

[7] D. Griggs, J. Blacic, Quartz: Anomalous weakness of synthetic crystals, Science 147 (3655) (1965) 292–295.

[8] D. Griggs, J. Blacic, J. Christie, A. McLaren, F. Frank, Hydrolytic weakening of quartz crystals., Science (New York, NY) 152 (3722) (1966) 674–674.

[9] D. Griggs, Hydrolytic weakening of quartz and other silicates, Geophysical Journal International 14 (1-4) (1967) 19–31.

[10] A. McLaren, R. Cook, S. Hyde, R. Tobin, The mechanisms of the formation and growth of water bubbles and associated dislocation loops in synthetic quartz, Physics and Chemistry of Minerals 9 (1983) 79–94.

[11] R. D. Aines, G. R. Rossman, Water in minerals? a peak in the infrared, Journal of Geophysical Research: Solid Earth 89 (B6) (1984) 4059–4071.

[12] N. G. Stenina, Water-related defects in quartz, Bulletin of Geosciences 79 (4) (2004) 251–268.

[13] R. Stalder, J. Konzett, Oh defects in quartz in the system quartz–albite–water and granite–water between 5 and 25 kbar, Physics and Chemistry of Minerals 39 (2012) 817–827.

[14] M. C. Jollands, M. Blanchard, E. Balan, Structure and theoretical infrared spectra of oh defects in quartz, European Journal of Mineralogy 32 (3) (2020) 311–323.

[15] J. D. Blacic, J. M. Christie, Plasticity and hydrolytic weakening of quartz single crystals, Journal of Geophysi-

cal Research: Solid Earth 89 (B6) (1984) 4223–4239.

[16] P. Cordier, J. C. Doukhan, Water speciation in quartz: a near infrared study, American Mineralogist 76 (3-4) (1991) 361–369.

[17] A. Post, J. Tullis, The rate of water penetration in experimentally deformed quartzite: implications for hydrolytic weakening, Tectonophysics 295 (1-2) (1998) 117–137.

[18] A. Müller, Cathodoluminescence and characterisation of defect structures in quartz with applications to the study of granitic rocks, Ph.D. thesis, Niedersächsische Staats-und Universitätsbibliothek Göttingen (2000).

[19] J. McConnell, J. Lin, V. Heine, The solubility of [4h] si defects in α-quartz and their role in the formation of molecular water and related weakening on heating, Physics and Chemistry of Minerals 22 (6) (1995) 357–366.

[20] J. Purton, R. Jones, M. Heggie, S. Oberg, C. Catlow, Ldf pseudopotential calculations of the α-quartz structure and hydrogarnet defect, Physics and chemistry of minerals 18 (1992) 389–392.

[21] N. H. de Leeuw, Density functional theory calculations of hydrogen-containing defects in forsterite, periclase, and α-quartz, The Journal of Physical Chemistry B 105 (40) (2001) 9747–9754.

[22] A. Rosa, A. El-Barbary, M. Heggie, P. Briddon, Structural and thermodynamic properties of water related defects in α-quartz, Physics and Chemistry of Minerals 32 (2005) 323–331.

[23] E. B. Tadmor, R. E. Miller, Modeling materials: continuum, atomistic and multiscale techniques, Cambridge University Press, 2011.

[24] D. Choudhuri, S. G. Srinivasan, Density functional theory-based investigations of solute kinetics and precipitate formation in binary magnesium-rare earth alloys: A review, Computational Materials Science 159 (2019) 235–256.

[25] M. Mendelev, F. Zhang, Z. Ye, Y. Sun, M. Nguyen, S. Wilson, C. Wang, K. Ho, Development of interatomic potentials appropriate for simulation of devitrification of al90sm10 alloy, Modelling and Simulation in Materials Science and Engineering 23 (4) (2015) 045013.

[26] M. P. Allen, D. J. Tildesley, Computer simulation of liquids, Oxford university press, 2017.

[27] H. Wilkinson, B. Boyd, J. M. O'Connell, R. Knox, A. J. Rinehart, B. S. Majumdar, D. Choudhuri, Factors controlling heteroepitaxial phase formation at intermetallic-al3sc/liquid interfaces, Journal of Applied Physics

133 (12) (2023).

[28] A. Groß, Reactions at surfaces studied by ab initio dynamics calculations, Surface science reports 32 (8) (1998) 291–340.

[29] H. Hu, W. Yang, Free energies of chemical reactions in solution and in enzymes with ab initio quantum mechanics/molecular mechanics methods, Annu. Rev. Phys. Chem. 59 (2008) 573–601.

[30] J. Blumberger, M. Sprik, Ab initio molecular dynamics simulation of the aqueous ru2+/ru3+ redox reaction: The marcus perspective, The Journal of Physical Chemistry B 109 (14) (2005) 6793–6804.

[31] T. Wang, F. Zhang, L. Yang, X. Fang, S. Zhou, M. Kramer, C. Wang, K. Ho, R. Napolitano, A computational study of diffusion in a glass-forming metallic liquid, Scientific reports 5 (1) (2015) 1–9.

[32] D. Choudhuri, B. S. Majumdar, H. Wilkinson, Investigation of in-liquid ordering mediated transformations in al-sc via ab initio molecular dynamics and unsupervised learning, Physical Review Materials 6 (10) (2022) 103406.

[33] D. Marx, J. Hutter, Ab initio molecular dynamics: basic theory and advanced methods, Cambridge University Press, 2009.

[34] R. M. Martin, Electronic structure: basic theory and practical methods, Cambridge university press, 2020.

[35] G. Kresse, J. Hafner, Ab initio molecular dynamics for liquid metals, Physical Review B 47 (1) (1993) 558.

[36] G. Kresse, J. Hafner, Ab initio molecular-dynamics simulation of the liquid-metal–amorphous-semiconductor transition in germanium, Physical Review B 49 (20) (1994) 14251.

[37] G. Kresse, J. Furthmüller, Efficient iterative schemes for ab initio total-energy calculations using a plane-wave basis set, Physical review B 54 (16) (1996) 11169.

[38] G. Kresse, D. Joubert, From ultrasoft pseudopotentials to the projector augmented-wave method, Physical review b 59 (3) (1999) 1758.

[39] J. P. Perdew, K. Burke, M. Ernzerhof, Generalized gradient approximation made simple, Physical review letters 77 (18) (1996) 3865.

[40] J. P. Perdew, K. Burke, M. Ernzerhof, Generalized gradient approximation made simple [phys. rev. lett. 77, 3865 (1996)], Phys. Rev. Lett 78 (7) (1997) 1396–1396.

[41] M. Tuckerman, Statistical mechanics: theory and molecular simulation, Oxford university press, 2010.

[42] D. Frenkel, B. Smit, M. A. Ratner, Understanding molecular simulation: from algorithms to applications, Vol. 2, Academic press San Diego, 1996.

[43] H. Tanaka, K. Nakanishi, N. Watanabe, Constant temperature molecular dynamics calculation on lennard-jones fluid and its application to watera, The Journal of Chemical Physics 78 (5) (1983) 2626–2634.

[44] R. Freitas, E. J. Reed, Uncovering the effects of interface-induced ordering of liquid on crystal growth using machine learning, Nature communications 11 (1) (2020) 1–10.

[45] A. Gross, Ab initio molecular dynamics simulations of the o2/pt (1 1 1) interaction, Catalysis Today 260 (2016) 60–65.

[46] A. Groß, Hot atom chemistry: Oxygen at stepped platinum surfaces, Applied Surface Science Advances 9 (2022) 100240.

[47] E. Kelly, M. Seth, T. Ziegler, Calculation of free energy profiles for elementary bimolecular reactions by ab initio molecular dynamics: sampling methods and thermostat considerations, The Journal of Physical Chemistry A 108 (12) (2004) 2167–2180.

[48] E. Weinan, D. Li, The andersen thermostat in molecular dynamics, Communications on pure and applied mathematics 61 (1) (2008) 96–136.

[49] S.-Y. Yang, P. Fleurat-Lessard, I. Hristov, T. Ziegler, Free energy profiles for the identity sn2 reactions cl-+ ch3cl and nh3+ h3bnh3: a constraint ab initio molecular dynamics study, The Journal of Physical Chemistry A 108 (43) (2004) 9461–9468.

[50] M. Rang, G. Kresse, First-principles study of the melting temperature of mgo, Physical Review B 99 (18) (2019) 184103.

[51] R. Réocreux, C. Michel, P. Fleurat-Lessard, P. Sautet, S. N. Steinmann, Evaluating thermal corrections for adsorption processes at the metal/gas interface, The Journal of Physical Chemistry C 123 (47) (2019) 28828–28835.

[52] S. Amokrane, A. Ayadim, L. Levrel, N. Jakse, Pair structure, diffusion and pressure in liquid cuzr alloys from ab initio simulations: assessing the sensitivity to the energy cutoff, Modelling and Simulation in Materials

Science and Engineering 30 (3) (2022) 035010.

[53] S. Grimme, Semiempirical gga-type density functional constructed with a long-range dispersion correction, Journal of computational chemistry 27 (15) (2006) 1787–1799.

[54] T. Bucko, J. Hafner, S. Lebègue, J. G. Angyán, Improved description of the structure of molecular and layered crystals: ab initio dft calculations with van der waals corrections, The Journal of Physical Chemistry A 114 (43) (2010) 11814–11824.

[55] N. Dzade, A. Roldan, N. H. de Leeuw, The surface chemistry of no x on mackinawite (fes) surfaces: a dft-d2 study, Physical Chemistry Chemical Physics 16 (29) (2014) 15444–15456.

[56] K. Ogata, Y. Takeuchi, Y. Kudoh, Structure of α-quartz as a function of temperature and pressure, Zeitschrift für Kristallographie-Crystalline Materials 179 (1-4) (1987) 403–414.

[57] J. Glinnemann, H. King Jr, H. Schulz, T. Hahn, S. La Placa, F. Dacol, Crystal structures of the low-temperature quartz-type phases of sio2 and geo2 at elevated pressure, Zeitschrift für Kristallographie-Crystalline Materials 198 (1-4) (1992) 177–212.

[58] J. Kim-Zajonz, S. Werner, H. Schulz, High pressure single crystal x-ray diffraction study on α-quartz, Zeitschrift Für Kristallographie-Crystalline Materials 214 (6) (1999) 324–330.

[59] S. M. Antao, I. Hassan, J. Wang, P. L. Lee, B. H. Toby, State-of-the-art high-resolution powder x-ray diffraction (hrpxrd) illustrated with rietveld structure refinement of quartz, sodalite, tremolite, and meionite, The Canadian Mineralogist 46 (6) (2008) 1501–1509.

[60] L. Levien, C. T. Prewitt, D. J. Weidner, Structure and elastic properties of quartz at pressure, American Mineralogist 65 (9-10) (1980) 920–930.

[61] Z. Xuefen, L. Guiwu, W. Xiaoming, Y. Hong, Molecular dynamics investigation into the adsorption of oil–water–surfactant mixture on quartz, Applied surface science 255 (13-14) (2009) 6493–6498.

[62] T. Goumans, A. Wander, W. A. Brown, C. R. A. Catlow, Structure and stability of the (001) α-quartz surface, Physical Chemistry Chemical Physics 9 (17) (2007) 2146–2152.

[63] K. Momma, F. Izumi, Vesta: a three-dimensional visualization system for electronic and structural analysis, Journal of Applied crystallography 41 (3) (2008) 653–658.

[64] J. Götze, Y. Pan, A. Müller, Mineralogy and mineral chemistry of quartz: A review, mineralogical magazine 85 (5) (2021) 639–664.

[65] A. Stukowski, Visualization and analysis of atomistic simulation data with OVITO–the Open Visualization Tool, Modelling and Simulation in Materials Science and Engineering 18 (1) (2010) 015012.

[66] R. DeHoff, Thermodynamics in materials science, CRC Press, 2006.

[67] J. M. Haile, Molecular dynamics simulation: elementary methods, John Wiley & Sons, Inc., 1992.

[68] D. Choudhuri, Y. Zheng, T. Alam, R. Shi, M. Hendrickson, S. Banerjee, Y. Wang, S. Srinivasan, H. Fraser, R. Banerjee, Coupled experimental and computational investigation of omega phase evolution in a high misfit titanium-vanadium alloy, Acta Materialia 130 (2017) 215–228.

[69] D. Choudhuri, Local structure and bonding environment of intermetallic $\beta 1$ precipitate phase nucleus in binary mg-nd, Computational Materials Science 187 (2021) 110111.

[70] K. L. Milton, T. R. Durrant, T. Cobos Freire, A. L. Shluger, Difference in structure and electronic properties of oxygen vacancies in α-quartz and α-cristobalite phases of sio2, Materials 16 (4) (2023) 1382.

[71] D. Choudhuri, A. CampBell, Interface dominated deformation mechanisms in two-phase fcc/b2 nanostructures: Nishiyama-wasserman vs. kurdjumov-sachs interfaces, Computational Materials Science 177 (2020) 109577.

[72] A. Katz, Hydrogen in alpha-quartz, Philips Res. Reports 17 (1962) 136–137.

[73] J. Bachheimer, An investigation into hydrogen stability in synthetic, natural and air-swept synthetic quartz in air temperatures up to 1100 c, Journal of Physics and Chemistry of Solids 59 (5) (1998) 831–840.

[74] A. Kronenberg, S. Kirby, R. Aines, G. Rossman, Solubility and diffusional uptake of hydrogen in quartz at high water pressures: implications for hydrolytic weakening, Journal of Geophysical Research: Solid Earth 91 (B12) (1986) 12723–12741.

[75] N. Binggeli, J. R. Chelikowsky, Structural transformation of quartz at high pressures, Nature 353 (6342) (1991) 344–346.

[76] S. Munetoh, T. Motooka, K. Moriguchi, A. Shintani, Interatomic potential for si–o systems using tersoff parameterization, Computational Materials Science 39 (2) (2007) 334–339.

[77] D. Choudhuri, B. S. Majumdar, Structural changes during crystallization and vitrification of dilute fcc-based

binary alloys, Materialia 12 (2020) 100816.

[78] M. Probert, An ab initio study of xenon retention in α-quartz, Journal of physics: Condensed matter 22 (2) (2009) 025501.

[79] S. L. Dudarev, G. A. Botton, S. Y. Savrasov, C. Humphreys, A. P. Sutton, Electron-energy-loss spectra and the structural stability of nickel oxide: An lsda+ u study, Physical Review B 57 (3) (1998) 1505.

[80] E. Hand, Hidden hydrogen, Science (New York, NY) 379 (6633) (2023) 630–636.

[81] B. K. Atkinson, Subcritical crack growth in geological materials, Journal of Geophysical Research: Solid Earth 89 (B6) (1984) 4077–4114.

[82] M.-C. Eppes, R. Keanini, Mechanical weathering and rock erosion by climate-dependent subcritical cracking, Reviews of Geophysics 55 (2) (2017) 470–508.

[83] Y. Nara, H. Yamanaka, Y. Oe, K. Kaneko, Influence of temperature and water on subcritical crack growth parameters and long-term strength for igneous rocks, Geophysical Journal International 193 (1) (2013) 47–60.

[84] M. Stipp, J. Tullis, H. Behrens, Effect of water on the dislocation creep microstructure and flow stress of quartz and implications for the recrystallized grain size piezometer, Journal of Geophysical Research: Solid Earth 111 (B4) (2006).

[85] S. L. Brantley, S. R. Crane, D. A. Crerar, R. Hellmann, R. Stallard, Dissolution at dislocation etch pits in quartz, Geochimica et Cosmochimica Acta 50 (10) (1986) 2349–2361.

[86] O. Jaoul, J. Tullis, A. Kronenberg, The effect of varying water contents on the creep behavior of heavitree quartzite, Journal of Geophysical Research: Solid Earth 89 (B6) (1984) 4298–4312.

[87] I. N. MacInnis, S. L. Brantley, The role of dislocations and surface morphology in calcite dissolution, Geochimica et Cosmochimica Acta 56 (3) (1992) 1113–1126.

[88] D. Mainprice, O. Jaoul, A transmission electron microscopy study of experimentally deformed quartzite with different degrees of doping, Physics of the Earth and Planetary Interiors 172 (1-2) (2009) 55–66.

[89] M. E. Malmström, G. Destouni, S. A. Banwart, B. H. Strömberg, Resolving the scale-dependence of mineral weathering rates, Environmental science & technology 34 (7) (2000) 1375–1378.

[90] N. Carter, A. Kronenberg, J. Ross, D. Wiltschko, Control of fluids on deformation of rocks, Geological Society,

London, Special Publications 54 (1) (1990) 1–13.

[91] M. Faccenda, Water in the slab: A trilogy, Tectonophysics 614 (2014) 1–30.

[92] H. O'Ghaffari, M. Peč, T. Mittal, U. Mok, H. Chang, B. Evans, Microscopic defect dynamics during a brittle-to-ductile transition, Proceedings of the National Academy of Sciences 120 (42) (2023) e2305667120.

[93] T.-f. Wong, P. Baud, The brittle-ductile transition in porous rock: A review, Journal of Structural Geology 44 (2012) 25–53.

[94] R.-F. Ge, S. A. Wilde, W.-B. Zhu, X.-L. Wang, Earth's early continental crust formed from wet and oxidizing arc magmas, Nature (2023) 1–6.

[95] D. Höning, H. Hansen-Goos, A. Airo, T. Spohn, Biotic vs. abiotic earth: A model for mantle hydration and continental coverage, Planetary and Space Science 98 (2014) 5–13.

[96] O. Grasset, J. Castillo-Rogez, T. Guillot, L. Fletcher, F. Tosi, Water and volatiles in the outer solar system, Space Science Reviews 212 (2017) 835–875.

[97] J. P. Greenwood, S.-i. Karato, K. E. Vander Kaaden, K. Pahlevan, T. Usui, Water and volatile inventories of mercury, venus, the moon, and mars, Space Science Reviews 214 (2018) 1–39.

[98] H. Behrens, Hydrogen defects in feldspars: defect properties and implications for water solubility in feldspar, Physics and Chemistry of Minerals 48 (2021) 1–22.

[99] H. Behrens, Hydrogen defects in feldspars: alkali-supported dehydrogenation of sanidine, Physics and Chemistry of Minerals 50 (3) (2023) 18.

[100] P. William, J. De Paula, J. Keeler, Atkins' Physical Chemistry, Oxford University Press, 2019.